Article:

The development and evaluation of a parameter-free circuit-based model of bipolar membrane electrodialysis for process design and optimisation

Jack Ledingham [a,*], Kyra L. Sedransk Campbell [a], Ben in 't Veen [b], Lucas Keyzer [b], Ngai Yin Yip [c,d], Alasdair N. Campbell [a]

[a] Department of Chemical and Biological Engineering, The University of Sheffield, Sheffield S1 4AA, United Kingdom
[b] Shell Global Solutions International B.V
[c] Department of Earth and Environmental Engineering, Columbia University, New York 10027-6623, United States
[d] Columbia Water Center, Columbia University, New York 10027-6623, United States

ARTICLE INFO

ABSTRACT

Bipolar membrane electrodialysis (BPMED) is an emerging electromembrane technology which has the potential to replace existing pH manipulation process units among others and take advantage of the benefits posed by process electrification. The development of robust and flexible process models of BPMED for design and optimisation is paramount in derisking potential instillations and improving commercial viability. Herein, a circuit-based model of BPMED is presented which avoids reliance on empirical fitting parameters and training data. The resulting model is flexible enough that extension to account for added complexities may be readily adopted. The mass transfer and electrical resistance of six different domains (three membranes and three streams) were computed by applying fundamental laws such as Ohm's law and Faraday's first law. Acid-base reactions and their effect releasing current within the membranes were also considered. Furthermore, the stack model can be readily embedded in a broader process model. To this end, the stack model is applied to a recirculating-batch experiment using a delayed differential material balance to account for dead-time within the tubing and measurement flow-cells. Two orthogonal methods of experimental validation were conducted to assess the performance of the model over a range of concentrations and applied voltages. These involved running a recirculating-batch experiment and collecting current–voltage polarisation data, respectively, and both showed good agreement with the model predictions. Overall, a robust model of BPMED has been produced which is able to accurately predict system performance and will prove useful for the design and optimisation of industrial systems.

1. Introduction

In recent decades, there has been a substantial and enduring decrease in the cost of renewable electricity from solar and onshore wind farms, primarily resulting from huge reductions in their construction costs [1]. Consequently, the levelized cost of electricity (LCOE) from wind and solar farms is now lower than from fossil fuels. Further, between 2021 and 2022, the LCOE of onshore wind and solar fell by 5 % and 3 %, respectively, suggesting that costs will continue to decrease. Globally, industrial processes account for more than a third of energy consumption [2] and more than a fifth of greenhouse gas emissions [3]. As such, the electrification of industrial processes has the potential to provide myriad benefits both in terms of process economics and sustainability

[4]. However, there are several challenges inhibiting the widespread adoption of electrified process units including the availability of suitable replacement technologies, the high capital costs of these less mature technologies, and the risk averse nature of industry [5]. Much of the focus of electrification revolves around process heat as this consumes a substantial amount of energy and has relatively mature replacement technologies. Separation processes and chemical reactors have historically been much more challenging to electrify. Electromembrane processes will be instrumental in the electrification of many industries as they have a wide range of capabilities in both mass transfer and electrochemical reactions. This makes them excellent as both reactors and separators, often concurrently. Further, the direct transfer of the electrical energy to the unit's functionality makes electromembrane processes highly tuneable and easily controllable.

Nomenclature

Latin Symbol

A	membrane physical parameter collection
A_a, A_c	Tafel slope parameters
AAD	average absolute difference
b	Wien effect dimensionless parameter
C	concentration
C_{fix}	fixed charge concentration
C_R	reservoir concentration
D	diffusivity
d	intermembrane distance
E	electric field strength
e	charge of an electron
F	Faraday's constant
f_w	water (void) fraction
G_0, E_{bp}	bipolar overpotential parameters
i	current density
i_{0a}, i_{0c}	Tafel exchange current density parameters
i_e	effective current density
J	ion flux
J_r	reaction flux
k_B	Boltzmann's constant
k_f, k_r	forward and reverse kinetic rate constants
K_w	water dissociation equilibrium constant
N_A	Avogadro's number
n_c	number of cell pairs
N_o	number of observations
R	resistance
R_g	gas constant
S	like-charge selectivity
T	temperature
t	temporal dimension
$\bar{t}$	transport number
t_p	membrane permeation time

u	velocity
V	voltage
V_R	reservoir volume
x	spatial dimension
z	charge number
ΔpH	pH difference across the bipolar junction

Greek Symbol

α	flux directionality parameter
β	reaction handling parameter
ε	permittivity
η	overpotential
θ	Coefficient of the summation of infinite vectors
κ	conductivity
μ	ion mobility
ν	ion stoichiometry
ξ	extent of reaction
τ	time delay
Φ	electric potential
$\chi, \bar{\chi}$	experimental/model predicted variable value

Subscript

0	initial/intrinsic value
bp	bipolar junction
$cell$	referring to the repeating unit cell
co	set of membrane co-ions
ct	set of membrane counterions
ec	end chamber
eq	equilibrium
$i(= Na, Cl, H, OH)$	ionic species
$j(= d, a, b)$	stream
$m(= AEM, CEM, BPM)$	membrane
s	referring to solution domain
$stack$	referring to the entire stack

The desire to manipulate pH is ubiquitous in chemical processes both to optimise process unit conditions and to neutralise waste effluents prior to discharge. At present, the most common industrial method of pH control involves dosing chemical additives, such as NaOH and HCl in a 'feed-and-bleed' configuration. Sophisticated control loops are required due to the logarithmic nature of pH and its sensitivity to strongly acidic or alkaline substances. Chemical dosing is simple and effective, but involves complex supply chains, increasing the economic and environmental burden. Here, electromembrane processes are uniquely poised to offer an advantageous alternative.

Bipolar membrane electrodialysis (BPMED) is an emerging electromembrane technology which provides an electrochemical alternative to existing pH manipulation process units [6]. The unique structure of BPMED systems allows for the treatment and valorisation of industrial wastewaters by concurrent resource recovery and pH adjustment. In BPMED, an electric field is simultaneously used to drive the transport of ions across ion exchange membranes (IEMs) between flowing streams and to induce water splitting into protons and hydroxide ions. The structure of a BPMED unit, known as a stack, is essentially an extension of conventional electrodialysis (ED) with the addition of a bipolar membrane (BPM).

The functionality of a BPM is to induce water splitting, which is achieved by laminating two oppositely charged IEM layers together with a catalyst at the interface [7]. These layers are a cation exchange layer (CEL) and anion exchange layer (AEL), which are permeable only to cations and anions, respectively. Theoretically, no ions can permeate through the BPM between the acid and base streams due to its composition. Only neutral species, such as water molecules, may diffuse into the BPM domain. However, to maintain continuity of current, ions must flow through the BPM. When a strong enough electric field is applied (on the order of 1 V per BPM), water splitting is initiated at the bipolar interface and protons and hydroxide ions are transported through the CEL and AEL of the BPM, respectively.

As with ED, the BPMED stack consists of many repeating unit cells which are comprised of streams and membranes (Fig. 1). The standard repeating unit of a BPMED stack consists of three membranes: an anion exchange membrane (AEM), a cation exchange membrane (CEM), and the BPM. Three different saline streams flow tangentially between these membranes in channels created by spacers. The stream between the AEM and CEM is known as the diluate or salt. Anions and cations within the diluate streams are driven by the electric field in opposite directions through the AEM and CEM, respectively. The acid stream receives the anions from the diluate stream and protons from the BPM. Conversely, the base stream receives the diluate's cations as well as hydroxide ions from the BPM. As such, the salt initially present within the diluate is converted into an acid and a base in different streams. To exemplify this, an NaCl feed can be converted into highly concentrated NaOH and HCl product streams. The limiting factors controlling how concentrated the acid and base can become are the membrane selectivity, the membrane stability, and the diluate feed concentration.

At present, there are a great number of publications which explore potential applications of BPMED in industry [8]. One of the most
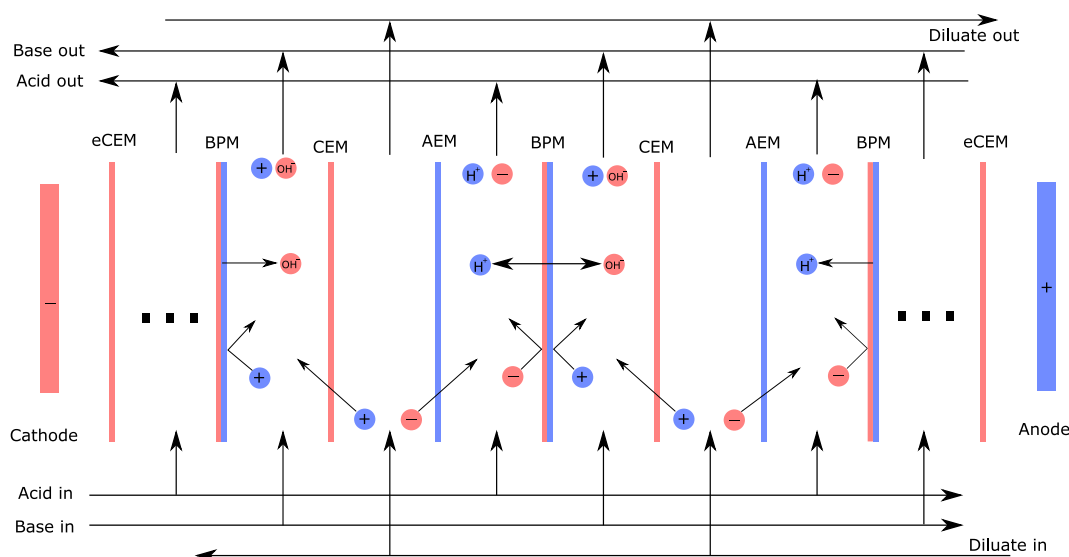
Fig. 1. A schematic representation of BPMED showing the four membrane types (AEM, CEM, BPM, eCEM), and three stream types (acid, base, diluate) as well as an ideal representation of how ions are trasnfered. A repeating element of two cell triplets is shown between the electrodes. Positive charges are shown in blue and negative charges in red. (For interpretation of the references to colour in this figure legend, the reader is referred to the web version of this article.)

prevalent is for the electrochemical recovery of CO_2 capture solvents [9]. The regeneration of capture solutions is an energy intensive process which typically involves heating the solution in a stripper column until the chemical equilibrium is thermally driven to the gaseous form of CO_2. With BPMED, the same equilibrium can be electrochemically driven by acidification of the stream. Further, BPMED has also been demonstrated to be practicable in the recovery of deep eutectic solvents (DES) used to pre-treat lignocellulosic biomass to increase digestibility prior to fermentation [10]. Here, the BPMED unit cell consists of only a BPM and AEM and is used to concurrently separate the DES and control its pH. Beyond solvent recovery, BPMED has been demonstrated in the recovery of copper from electroplating sludge [11]. The copper was successfully recovered by using the protons generated by the BPMED to balance the pH in the waste sludge. The current best alternate approach to this involves chemical or biological leaching which are environmentally hazardous and slow, respectively.

Despite the myriad potential applications explored academically, there are very few industrially implemented examples of BPMED [12]. This primarily stems from the risk-averse nature of industry and the fact that tried-and-tested technologies typically benefit from lower costs and greater reliability. Bipolar membranes are also very expensive, on the order of 1000 $/m^2. This far exceeds the costs of other IEMs, which are typically between 50 and 100 $/m^2 [13]. Technological advancements in BPM manufacturing are likely to close this gap to a degree but would need to be funded by considerable commercial investment. At present, other cost-saving methods and optimisations are needed in order for BPMED to gain traction. As such, process intensification to reduce the size of units would greatly improve the commercial feasibility.

A cost optimisation for electromembrane processes exists through variation of the applied voltage. In general, the desired overall current is pre-determined as this is directly proportional to the total amount of ions transferred between the streams. A higher voltage leads to a higher current density (Ohm's law) and thus a lower membrane area and stack size is required, reducing the capital expenditure. However, a higher voltage also increases the specific power consumption, increasing the operating expenditure. Mathematical modelling of BPMED can be used to optimise the size of a stack and consequently de-risk industrial adoption of the technology. However, due to the myriad concurrent phenomena at the nano, micro, and macro scale, electromembrane technologies, and especially BPMED, can be very challenging to model accurately. Herein, a robust mathematical model of a BPMED process is

to be developed which can adequately represent phenomena over a wide range of process conditions to allow for comprehensive design and optimisation.

Relative to conventional ED, there are very few published studies concerning BPMED modelling. A recent publication by Culcasi *et al.* [14] evaluated twelve existing BPMED models, classifying them based on their solution methods and the phenomena considered and neglected. It was made clear that, as with conventional ED, there are a wide range of different BPMED model formulations. Phenomena such as diffusion, osmosis, back-migration, shunt currents, and concentration polarisation are considered by some models but not by others. Despite this, all models show at least a reasonable agreement with validation experiments. The individual phenomena mentioned are generally very difficult to model accurately without the use of empirical fitting parameters. For example, concentration polarisation is highly dependent on the hydrodynamic environment as it determines the thickness of the boundary layers where concentration gradients form. The degree of turbulence provided by the spacer directly influences the boundary layer thickness, which in turn is strongly controlled by the geometry of the spacer. Since modelling this is ambiguous, fitting parameters are employed. Consequently, it is very easy for the complex phenomena included to confound others, leading to them inadvertently compensating for each other's inaccuracies. With more phenomena and fitting parameters included, it becomes ever easier to find local minima when fitting parameters, especially when limited experimental data sets are considered. As such, the model developed in this work will completely avoid the use of fitting parameters and training data. To achieve this, only phenomena that can be directly modelled and which use readily accessible parameters are included.

For many existing BPMED models, experimental validation is conducted as a means of parameter estimation [14–20]. This is done to either find values of parameters that are otherwise difficult to predict (e. g. membrane diffusivities, transport numbers, temperature dependence of conductivity), or used to gain insight into experimental results (e.g. finding the current efficiency, or membrane resistance). This is useful for improving the accuracy in the range where they are experimentally validated but limits generalisation. Extrapolation is often necessary for process design and optimisation due to the time-intensive nature of experimental studies. Additionally, many existing models use lumped empirical parameters to simplify equations and parameter estimation, further obfuscating the model insights. In this work, experimental and

modelling results are collected completely separately, and compared directly, providing a sincere and robust evaluation of the model.

The Nernst-Planck equation is very commonly used to model multidimensional concentration fields in both conventional ED and BPMED. Here, an overall flux is computed by summing contributions from diffusive, electrophoretic, and convective constituents [21]:

$$\boldsymbol{J}_i = D_i \nabla C_i + u C_i + \mu_i z_i C_i \nabla \Phi \tag{1}$$

$$\nabla \bullet \boldsymbol{J}_i = 0 \tag{2}$$

In these equations, $\boldsymbol{J}_i$ is the overall flux vector of component i, D_i is its diffusivity, C_i its concentration, μ_i its mobility, z_i its charge number, $\boldsymbol{u}$ is the velocity vector, and Φ is the electric potential. A charge condition is required for closure of this model. The most common is the assumption of electroneutrality, where the sum of all charges at each spatial point (including the membrane) is zero. To model the water splitting effect of the Bipolar membrane, an equation for the second Wien effect is used, where the water dissociation constant is a function of the electric field strength [22,23].

$$K_w = C_H C_{OH} \tag{3}$$

$$K_w = \frac{k_f(E)}{k_r} \tag{4}$$

$$k_f(E) = k_{f,0} \left(1 + b + \frac{b^2}{3} + \frac{b^3}{18} + \frac{b^4}{180} + \cdots \frac{b^n}{(n+1)! n!/2^n} \right) \tag{5}$$

$$b = 0.09636 \frac{\nabla \Phi}{\varepsilon T^2} \tag{6}$$

Here, K_w is the water dissociation constant, k_f and k_r are the forward and reverse reaction rate constants for the dissociation of water, respectively, $k_{f,0}$ is the nominal forward reaction rate constant without the effect of the electric field, E is the electric field strength (negative gradient of electric potential), b is a dimensionless term dependent on the strength of the electric field, ε is the domain permittivity, and T is the temperature. The value of b will be greatest in locations where there is a large gradient of the electric potential, like at the bipolar junction and membrane-solution interfaces when approaching the limiting current density (LCD). Here, k_f sharply increases, leading to an increase in the rate of water splitting and the water dissociation equilibrium constant, thereby providing the H$^+$ and OH$^-$ ions. Water recombination is driven by an excess of H$^+$ and OH$^-$ ions which are transported in opposite directions due to their opposite charges. Due to this, and the fact that the reactions are fast, recombination typically occurs in a plane. One key strength of Nernst-Planck modelling is that the location of this plane can be discerned. Water dissociation and recombination reactions can either be modelled as dynamic by separately computing the forward and reverse reaction rates, or as an equilibrium which is constantly maintained. The former is much more computationally challenging due to the large reaction terms.

Ortega *et al.* [24] and Leon *et al.* [25] used a Nernst-Planck model in COMSOL Multiphysics to compute a two-dimensional concentration field across a three-channel BPMED cell. Wang *et al.* [26] used the same method but in an unspecified software. Results tend to be very granular, where the concentrations and fluxes of individual species as well as the electric potential, can be evaluated at every spatial point in the domain. As such, this modelling approach is excellent for investigating small scale phenomena which may or may not contribute significantly to overall performance. However, when these concentration profiles are used to calculate full scale performance, errors can aggregate, leading to poor predictability. Further, the 2D electrolyte domains do not account for the turbulent mixing provided by the netted membrane spacer, a key source of mass transfer in real electromembrane systems.

One-dimensional Nernst-Planck models are more common than 2D

models due to their greater simplicity [17,26,27]. Here, the dimension perpendicular to the membrane surface is either integrated out or ignored. Other methods of modelling mass transfer in BPMED beyond Nernst-Planck models typically include the incorporation of membrane permeabilities to compute ion fluxes [20,28].

Equivalent-circuit models are often used to model conventional ED but have rarely been applied to BPMED. In an equivalent-circuit model, the analogy between electrons moving in a circuit and the ions flowing in an electromembrane stack is leveraged. Fundamental laws such as Ohm's law and Faraday's first law are used to relate important macroscopic variables such as voltage, current density, electrical resistance, and ion flux. As such, these models are very robust, computationally inexpensive, directly applicable to macroscale processes, and can be very flexible. Additional sub-models are used to incorporate smaller-scale phenomena through the electrical resistance and material balance. Vera *et al.* [18] used an equivalent circuit model to model the deacidification of fruit juice using BPMED. Despite the high complexity of the media studied, a reasonable agreement between model predictions and experimental results was achieved. However, experiments were conducted to estimate model parameters such as the current efficiency and the membrane resistance, reducing the predictive power and hence generality of the model.

Previous work [29] has demonstrated the efficacy of a one-dimensional circuit-based modelling strategy for electromembrane processes, using conventional ED as a case study. Adaptability was a key driver in model development, where it was claimed that additional phenomena could be accounted for through modifications to the material balance and the cell resistance model. In this work, this claim is evaluated by using a similar modelling strategy for the development of model of BPMED which avoids the use of empirical fitting parameters. The model developed is then validated against a recirculating-batch experiment, using a moderately concentrated NaCl solution that could be reasonably expected in an industrial operation. Various phenomena such as diffusion, water permeation, concentration polarisation, and shunt currents were neglected due to their low impact at the conditions validated against and the difficulty of modelling them accurately without using empirical parameters. However, the flexibility of the model is such that they can easily be included if deemed necessary. The avoidance of empirical parameters ensures that the model has applicability over as wide a range of concentrations and scales as possible. The objective of this research is to provide a robust model framework which can be adapted to specific situations through the assumptions made.

2. Model formulation

Laboratory experiments of both conventional ED and BPMED are almost exclusively conducted on recirculating-batch systems (Fig. 2a). Separate reservoirs for the acid, base, and diluate are present, the conductivity and pH of which are typically measured over time. Further details about the experimental system being modelled can be found in Section 3. Conversely, industrial BPMED processes are typically operated in a continuous configuration, either as a once-through process or with a recycle stream. As with the previous work, the aim of the modelling approach detailed herein is to be applicable to all scales and all configurations of BPMED. As such, the presented model consists of three 'layers' (Fig. 2c), the outermost of which defines the overall BPMED process. Here, initial conditions are defined, overall material balances are solved, and global variables such as the current density and faradic efficiency are computed. In the middle layer, acid-base equilibria, the BPM voltage drop, and differential spatial material balances are computed along the flow path within the BPMED stack. The stack is imagined as many differential slices perpendicular to the direction of flow (Fig. 2b). Transport between channels is related to the applied voltage and changes in concentration along the flow path are computed from material balances. The electrical resistance of each differential volume is also computed here using the analogy of an electric circuit
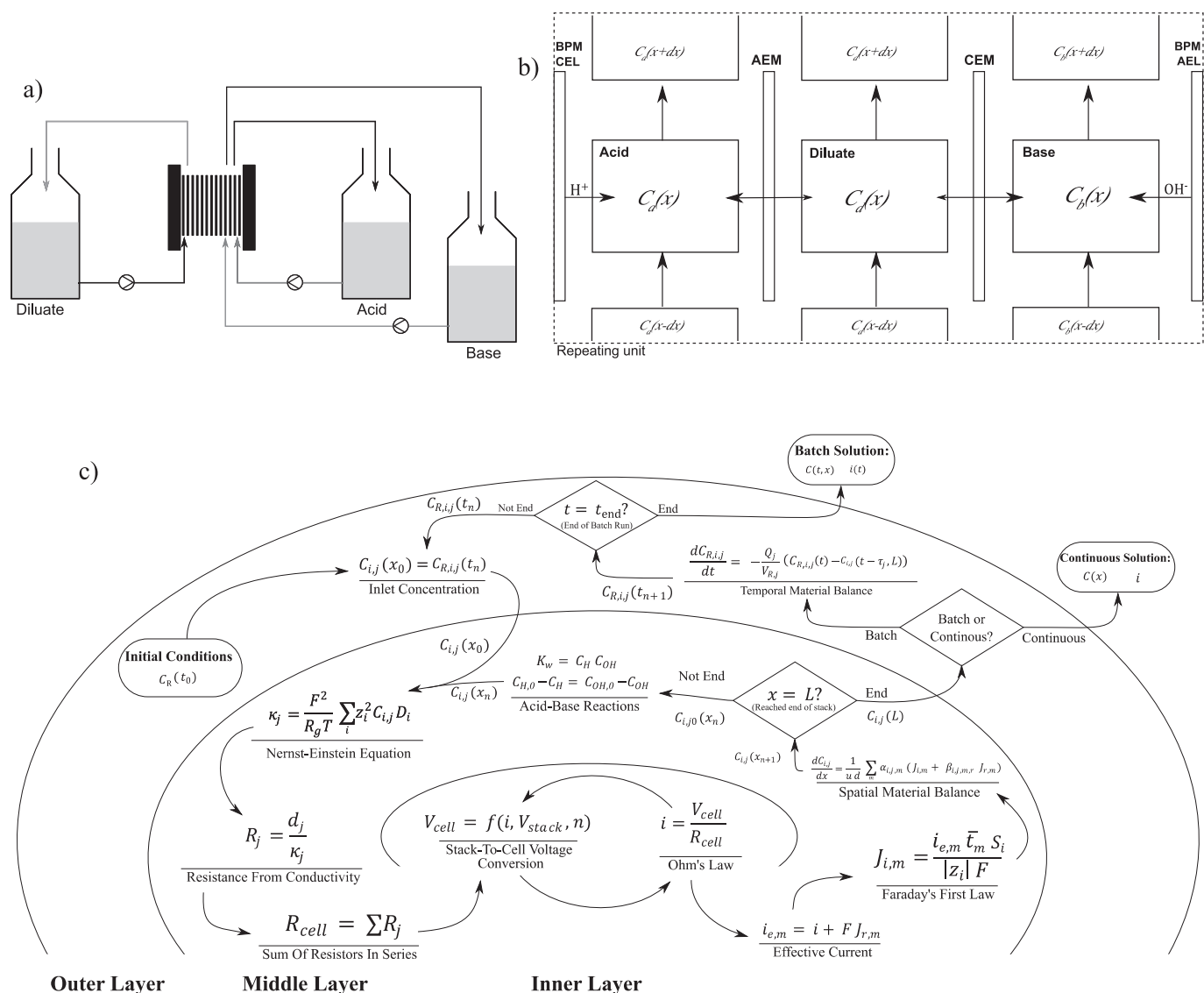
Fig. 2. A) a schematic representation of a recirculating batch bpmed system. streams from each of the three reservoirs are pumped around a circuit through the bpmed stack. b) a diagram of the differential volume slice used for the inner and middle layers within the model. indications of how ions permeate membranes are shown with horizontal lines, and the convective transfer between adjacent differential volumes is shown with vertical lines. c) a flow diagram showing the transfer of information within the layered model and the positioning of the equations. the difference between batch and continuous formulations is also shown.

with different resistive elements for each membrane and electrolyte. The resistance and cell voltage are then passed to the inner layer where the Tafel equation and Ohm's law are iteratively solved to find and return the current density of the differential slice. An 'effective' current density is computed for each transporting membrane which accounts for the current released by species reacting within the membrane domains. Once the effective current density is known, a modified form of Faraday's law which incorporates transport numbers and like-charge selectivities is used to compute the fluxes of each ion permeating each membrane. The fluxes are converted into concentration derivatives, assuming plug flow within the channels, after which the concentration at the next differential volume can be computed. Once internal concentration profiles are found, the stack outlet concentrations are passed back to the outer layer to be used in the overall material balance.

In this model, it is assumed that transmembrane diffusion and osmosis are negligible since they are at least two orders of magnitude slower than transport by electroconvection when operating under normal conditions. These assumptions are scrutinised in Section 3.1. Despite their neglect, the flexibility of the model is such that these

phenomena may be included through modifications to the material balances. This may prove necessary for processes where they cannot be neglected such as when a low voltage is applied and there is a very large *trans*-membrane concentration difference. Membrane boundary layers and concentration polarisation are also not considered due to the assumption of plug flow. These are strongly dependent on the hydrodynamic environment and membrane spacer geometry used, and thus require empirical models to capture them accurately. Further, below the LCD of the transporting membranes, where this model is solely applicable, its impact on process scale variables is limited.

This model of BPMED was implemented and solved in MATLAB R2022b. The explicit nature of this modelling strategy makes solving in programmes like MATLAB and Python particularly attractive and facilitates further development and modification. However, some modellers prefer using implicit methods in software such as gPROMS or COMSOL Multiphysics. As such, a generalised form of the model in its entirety has been presented as a system of differential and algebraic equations within an electronic supplementary information document.

2.1. Inner layer: Solving for current density

The goal of the inner-most layer is to determine a current density across a differential volume of a single cell of the BPMED stack given a cell resistance and stack voltage. A single unit cell triplet is here defined as a channel for each of the three streams (diluate, acid, and base) separated by an AEM, CEM and BPM (Fig. 2b). The analogy of an electric circuit is used, where each of these six constituent domains are resistive elements, and the transported ions are the charge carriers. Thus, the current density (i) perpendicular to the direction of fluid flow can be computed through Ohm's law [30].

$$i = \frac{V_{cell}}{R_{cell}} \tag{7}$$

Here, V_{cell} and R_{cell} are the voltage and electrical resistance across the unit cell, respectively. The cell resistance is provided by the middle layer, but the voltage across a cell pair is not yet known. It should be noted that the layout of the cell is chosen such that the voltage drop across the bipolar junction is not included in V_{cell}, making this the voltage which drives ion transport only. A voltage across the entire stack (V_{stack}) is provided by an external power supply and is constant for all differential volume slices. Since its value is typically set by design, it is assumed here to be known. The value of V_{cell} can be computed from V_{stack} by accounting for ancillary voltage drops from the electrode equilibrium potential (V_{eq}), the electrode overpotential (η), the water splitting potential at the bipolar interface (V_{bp}), and the voltage drop over the electrolyte end chambers (V_{ec}).

$$V_{cell} = \frac{1}{n_c}\left(V_{stack} - V_{eq} - \eta - V_{ec}\right) - V_{bp} \tag{8}$$

Here, n_c is the number of unit cells within the stack which divides the voltages relating to the entire stack between each of the cell pairs. The overpotential can be computed using the Tafel equation [31]:

$$\eta = A_a \log\left(\frac{i}{i_{0,a}}\right) + A_c \log\left(\frac{i}{i_{0,c}}\right) \tag{9}$$

where A and i_0 are well established empirical parameters found in literature dependent on the electrode material and reactions occurring. The voltage drop over the electrolyte chambers and end membranes is accounted for using Ohm's law

$$V_{ec} = 2i\left(R_{eCEM} + \frac{d_{ec}}{\sum_i C_{ec,i}\kappa_{mc,i}}\right) \tag{10}$$

Here, R_{eCEM} is the electrical resistance of the end cation exchange membranes, d_{ec} is the width of the end chamber in the direction of the electric field, $C_{ec,i}$ is the end chamber ion concentration of species i and $\kappa_{mc,i}$ is the molar conductivity of species i. A factor of two is present to account for both the anolyte and catholyte, which are assumed to provide the same electrical resistance. The resistance of the end chamber is assumed to be constant, but this could be altered.

The voltage drop across the bipolar membrane can be split into an equilibrium potential ($V_{bp,eq}$) and overpotential (η_{bp}), in the same way as electrode reactions are.

$$V_{bp} = V_{bp,eq} + \eta_{bp} \tag{11}$$

The equilibrium bipolar splitting voltage is the minimum voltage required across the bipolar junction to overcome the thermodynamic energy barrier and induce water splitting. According to Strathmann *et al.* [32], $V_{bp,eq}$ can be calculated from the Nernst equation, assuming a complete exclusion of co-ions within the BPM.

$$V_{bp,eq} = 2.3\frac{R_g T}{F}\Delta pH \tag{12}$$

Here, R_g is the ideal gas constant, T is the temperature, F is the Faraday constant, and ΔpH is the difference in pH across the bipolar junction. The pH inside the membrane is computed using the Donnan equilibrium and a charge balance, assuming only H^+ and OH^- ions are present inside the bipolar membrane [33].

$$C_{H,BPM} = 0.5\left(C_{fix} + \sqrt{C_{fix}^2 + 4\prod_i C_{i,a}}\right) \tag{13}$$

$$C_{OH,BPM} = 0.5\left(C_{fix} + \sqrt{C_{fix}^2 + 4\prod_i C_{i,b}}\right) \tag{14}$$

Here C_{fix} is the fixed ion concentration in the membrane and $C_{i,a}$ and $C_{i,b}$ are the concentration of species i in the acid and base chambers, respectively. The bipolar membrane overpotential is typically modelled as proportional to the current density, the proportionality constant of which is of Arrhenius type to account for the effect of temperature. A simple, but tested, relation proposed by Chen *et al.* [34] is:

$$i = \left(G_0 e^{-\frac{E_{bp}}{R_g T}}\right)\eta_{bp} \tag{15}$$

where G_0 and E_{bp} are kinetic parameters analogous to a pre-exponential factor and activation energy for a chemical reaction rate constant, respectively. The exact values of these parameters depend on the composition of the BPM in use. Most notably, they are dependent on the identity and loading of the catalyst employed at the bipolar junction. It should be noted that G_0 varies widely depending on the catalyst loading and can optimally be on the order of 10^{10} S m^{-2}. The activation energy for water splitting in pure water is 69 kJ/mol. The presence of the catalyst at the bipolar junction reduces this to around 25 – 30 kJ/mol. For BPMs operated at 298 K and a current density of 100 A m^{-2}, the overpotential is only 1.8 mV. Hence, for a well-designed BPM, the bipolar overpotential can often be neglected.

After each ancillary potential has been accounted for, it is possible to compute the cell voltage and current density. However, whilst the cell voltage has a linear dependence on the electrode overpotential, the electrode overpotential has a logarithmic dependence on the current density. Consequently, this set of equations must be solved iteratively. It is primarily for this reason that these computations are separated into their own layer of the model. The MATLAB function 'fzero' was used to loop over the inner layer equations and converge upon a solution for the current density and cell voltage.

Greater computational expediency was gained by selecting appropriate initial guesses for the current density when calling the fzero function. The value of the current density from the previous inner layer solution was used for this, as they would naturally be close in value.

Special consideration was given for the case that V_{cell} was computed as negative in equation (8). This would indicate that the applied potential was lower than $V_{eq} + V_{BP,0}$ and thus too low to drive any transport. In this case, V_{cell} was forced to be zero, resulting in zero current density and no flux.

2.2. Middle layer

The spatial differential material balance within the middle layer computes the concentration profiles of all ion species in each channel along the length of the flow path within the BPMED stack. Ultimately, the derivative of the concentration of species i in channel j with respect to spatial position $\left(\frac{dC_{i,j}}{dx}\right)$ is found from the concentrations in a differential slice across the stack. It is assumed that the channels are in plug flow and that the spacer nets take up a negligible amount of the internal channel volume.

The middle layer can be broken down into three primary functionalities:

I. Solve the acid-base equilibria and set all concentrations to their equilibrium values.
II. Compute the electric resistances of the electrolytes and membranes to be passed to the inner layer.
III. Find the fluxes of all ionic species once the current density is returned from the inner layer using Faraday's first law.

2.2.1. Acid-base equilibria

Acid-base speciation reactions are a distinctive characteristic of BPMED, and so must be numerically handled appropriately. Within this model, the effect of these reactions is determined before any other calculations can take place. Due to the rapid rate of water dissociation reactions (rate constant $\sim 10^8 \text{ mol}^{-1} \text{ m}^3 \text{ s}^{-1}$), it is assumed that all reactions are instantaneously brought to equilibrium. For the water speciation reaction within the channels, two equations are required. These are the water equilibrium equation and a material balance which represents the equivalent consumption/production of H^+ and OH^- ions:

$$K_w = C_H C_{OH} \tag{16}$$

$$\xi_{H/OH} = C_{H,0} - C_H = C_{OH,0} - C_{OH} \tag{17}$$

Here, K_w is the water dissociation constant, $\xi_{H/OH}$ is the extent of reaction (assuming the consumption of ions is positive), C_H and C_{OH} are the concentrations of H^+ and OH^- ions in the differential volume after the reaction has occurred, and $C_{H,0}$ and $C_{OH,0}$ are the theoretical concentrations after the ion transfer from the previous step has taken place but before the reaction has occurred. These equations can be combined to compute the extent of reaction within a differential slice as a function of the pre-reaction concentrations:

$$\xi_{H/OH} = \frac{1}{2} \left[(C_{H,0} + C_{OH,0}) - \sqrt{(C_{H,0} - C_{OH,0})^2 + 4K_w} \right] \tag{18}$$

Similar equations can be derived for any weak acid or base present in the streams. The post-reaction concentrations are used in the next steps to determine the electric resistances of the streams and membranes.

2.2.2. Electrical resistance

The cell electrical resistance is computed from the sum of the electrolyte and membrane resistances using a resistors-in-series approach. An analogy to an electric circuit is drawn with distinct resistive elements used for each of the membranes and electrolyte streams.

$$R_{cell} = \sum_j R_j + \sum_m R_m \tag{19}$$

Here, R_j is the electric resistance of channel j ($= d, a, b$), and R_m is the electric resistance of the domain of membrane m ($= AEM, CEM, BPM$). Note that for the BPM, only the resistance across the transporting domains of the CEL and AEL are considered here as the bipolar junction voltage drop is accounted for in equation (8).

These electric resistances are calculated in the same way as in previous work. Electrolyte resistances are computed from the conductivity (κ_j) and intermembrane distance (d_j) [21].

$$R_j = \frac{d_j}{\kappa_j} \tag{20}$$

The electrolyte conductivity can be computed by summing up contributions from individual ions and using the Nernst-Einstein equation [35]:

$$\kappa_j = \frac{F^2}{R_g T} \sum_i z_i^2 C_{i,j} D_{i,s} \tag{21}$$

Here, $C_{i,j}$ is the molar concentration of species i in channel j, and $D_{i,s}$ is its diffusivity in solution.

The membrane resistance is calculated in a similar way to the electrolyte resistance, but with a few key differences. The membrane conductivity (κ_m) is again computed using contributions from individual ions in the Nernst-Einstein equation.

$$\kappa_m = \frac{F^2}{R_g T} \sum_i z_i^2 C_{i,m} D_{i,m} \tag{22}$$

Here, $C_{i,m}$ is the concentration of species i within the membrane, and $D_{i,m}$ is its membrane diffusivity. As in the previous work, the Donnan equilibrium and electroneutrality equations are used to compute the membrane concentrations at the boundary with the electrolyte [36,37].

$$\prod_{i=1}^2 C_{i,j}^{\nu_i} = \prod_{i=1}^2 C_{i,m}^{\nu_i} \tag{23}$$

$$\sum_i z_i C_{i,j} = z_m C_{fix} + \sum_i z_i C_{i,m} \tag{24}$$

Here, ν_i is the stoichiometric coefficient of the ion within the salt and z_m is the charge number of the membrane (-1 for CEM and $+1$ for AEM). A form of equation (23) exists for every pairwise combination of ions. An alternate, non-ideal, formation of these equations exists where activity coefficients multiply each of the concentration terms. Through this, the inherent selectivity of membranes towards certain species may be considered.

Membrane diffusivities are computed using a model outlined by Fan *et al.* [38] which considers the electrostatic interactions between all transported ions and fixed charge groups. This model incorporates only easily accessible membrane properties such as the swelling degree (f_w) and the fixed charge concentration (C_{fix}), often provided by membrane manufacturers.

$$D_{i,m} = D_{i,s} \left(\frac{f_w}{2 - f_w} \right)^2 \exp\left(-A z_i^2 \right) \tag{25}$$

$$A = \frac{\theta e^4 N_A^{2/3}}{16 \pi^4 \varepsilon_m^2 k_B^2 T^2} C_{fix}^{2/3} \tag{26}$$

Other parameters in this model include a coefficient arising from the sum of infinite vectors (θ, 5.48 if fixed charges are assumed to be point charges, refer to the supporting information of [38] for more detail on this), the charge of an electron (e), Avogadro's number (N_A), the matrix permittivity (ε_m), and the Boltzmann constant (k_B).

For dilute external electrolytes, all parameters in equations (25) and (26) are constant, and so the membrane diffusivity is invariant. However, in concentrated solutions, osmotic deswelling causes the water content of the membrane (f_w) to decrease and the fixed charge concentration (C_{fix}) to increase, resulting in a reduction of the membrane diffusivity [39]. To account for this effect, additional equations are required to compute the change in membrane volume as a function of bathing solution concentration, such as the one proposed by Kozmai *et al.* [40]. However, for this application, membrane deswelling is neglected to avoid empirical fitting parameters and because validation was conducted in dilute NaCl solution.

Due to the changing internal concentration across the width of the membrane, the overall resistance is computed by finding the conductivities at both sides of the membrane and integrating, as in previous work:

$$R_m = \frac{d_m \ln\left(\frac{\kappa_{m,1}}{\kappa_{m,2}} \right)}{\kappa_{m,1} - \kappa_{m,2}} \tag{27}$$

It should be noted that this is not necessary for the two layers of the BPM,

which are assumed to have a flat concentration profile, resulting in the following equation for the BPM resistance:

$$R_{BPM} = \frac{R_g T}{F^2} \left(\frac{d_{AEL}}{D_{OH,AEL} C_{OH,AEL}} + \frac{d_{CEL}}{D_{H,CEL} C_{H,CEL}} \right) \tag{28}$$

After the resistances of the membranes and electrolytes are found, the cell resistance is computed and passed to the inner layer. The current density is then returned and used to find the ion flux.

2.2.3. Ion migratory flux

The current density returned by the inner layer is used to compute an ion flux which is ultimately converted into a concentration differential. For consistency, only the magnitude of the fluxes is considered here, and directionality is factored in later when computing the spatial derivative of the concentration. The simplest flux calculation is that for the bipolar membrane. It is assumed that there is total exclusion of external ions from the BPM and thus all current is carried by the water splitting products. Therefore, the water splitting flux (J_{BPM}) is equivalent to the flux of protons from the CEL of the BPM into the acid channel and of hydroxide ions from the AEL into the base channel. It is calculated using Faraday's first law:

$$J_{BPM} = \frac{i}{F} \tag{29}$$

A more complex approach is required for the selective transport membranes (AEM and CEM) due to the multitude of species and reactions potentially present. The flux magnitude through each transporting membrane ($J_{i,m}$, $m = AEM,CEM$) is computed separately for counterions and co-ions from the current density, again using Faraday's first law:

$$J_{i,m} = \frac{i_{e,m} \bar{t}_m S_{i,m}}{|z_i| F} \qquad \forall \ i \in ct \tag{30}$$

$$J_{i,m} = \frac{i_{e,m} (1 - \bar{t}_m) S_{i,m}}{|z_i| F} \qquad \forall \ i \in co \tag{31}$$

Here, *ct* is the set of species which are counterions in membrane *m* and *co* is the set of species that are co-ions. Instead of directly using the current density returned by the inner layer, an 'effective' current density (i_e) is used. This is to account for the additional current released by acid-base reactions within the membrane and is discussed further below.

Two important selectivity factors are present in this equation which relate the overall ion flux to that of an individual species. These are the transport number of the membrane ($\bar{t}_m$), and the like-charge selectivity of the species (S_i). The membrane transport number is defined as the ratio of the useful current carried by counterions to the total current carried across the membrane. As such, it varies between zero and unity and is analogous to both a selectivity and current efficiency for a single membrane. Hence, the co-ion flux has the ($1 - t_m$) term.

In previous work, a transport number model was presented which considers the transmembrane concentration ratio and an 'intrinsic' transport number. The value of the intrinsic transport number is often one provided by membrane manufacturers and is defined as the value measured when the transmembrane concentrations are equal. This model was derived considering the migratory flux term from the Nernst-Planck equation. A similar transport number model is used here which has been adapted to account for multiple competing co-ions and counterions.

$$\frac{1}{\bar{t}_m} = 1 + \frac{\sum_{i \in co} |z_i| C_{i,j}}{\sum_{i \in ct} |z_i| C_{i,d}} \left(\frac{1}{t_{m,0}} - 1 \right) \tag{32}$$

In this equation, the ratio of the *trans*-membrane equivalent concentrations accounts for the additional electrophoretic driving force when there is a higher normality on one side of the membrane. The channel (*j*) indicated in this equation is whichever one counterions are transported

into across membrane *m*. For the CEM, this is the base, and for the AEM this is the acid.

The selectivity between like charged ions (e.g., H^+ and Na^+) is defined as the fraction of counterion or co-ion flux corresponding to a single species. This can be computed from their relative electro-migration fluxes within the membrane as described in the Nernst-Planck equation (equation (1). Here, a similar development justification to the transport number model is used. For a single species, the electro-migratory flux ($J_{e,i}$) term is calculated by

$$J_{e,i} = z_i C_i \mu_{i,m} \nabla \Phi \tag{33}$$

where z_i is the ion charge number, $\mu_{i,m}$ is the ion mobility in the membrane, and $\nabla \Phi$ is the gradient of the electric potential. According to the Einstein-Smoluchowski relationship [35,41], ion mobility is proportional to diffusivity.

$$\mu_{i,m} = \frac{F}{R_g T} |z_i| D_{i,m} \tag{34}$$

Hence, the proportion of the counterion or co-ion flux carried by a single species can be found from simply summing the contributions of individual ions and taking a ratio. The electric potential gradient, temperature and gas constant conveniently cancel through.

$$S_{i \in ct} = \frac{z_i C_i D_i}{\sum_{i \in ct} z_i C_i D_i} \quad S_{i \in co} = \frac{z_i C_i D_i}{\sum_{i \in co} z_i C_i D_i} \tag{35,36}$$

A similar relationship it presented by Roux-de Balmann *et al.* [42]. As with the Donnan equations for computing membrane concentrations, these terms can be modified to account for the inherent selectivity that membranes have for certain species. This can be done with the inclusion of activity coefficients multiplying each concentration.

The necessity of an effective current density arises due to acid-base reactions occurring within the transporting membranes. For example, protons and hydroxide ions which both travel through the transporting membranes would meet at a plane and neutralise each other. Consequently, the *trans*-membrane current carried by acid-base active species is reduced, releasing additional current to be carried by all species (Fig. 3). The effective current density can be found from this additional current, which is equal to the reacting flux ($J_{r,m}$) multiplied by the Faraday constant. For the water recombination reaction, this is:

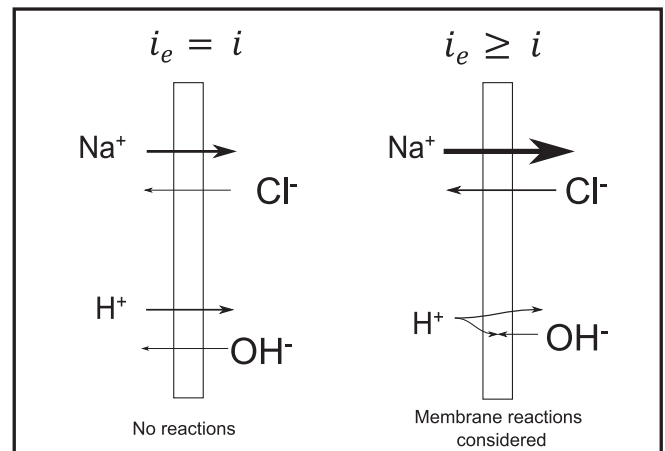$$J_{r,m} = \min\{J_{H,m}; J_{OH,m}\} \tag{37}$$

Fig. 3. A schematic representation of how acid-base reactions within the membrane domain releases additional current which is captured in an 'effective' current density (i_e). The size of the arrows is representative of the ion flux, but they are not to scale.

$$i_{e,m} = i + J_{r,m}F \qquad (38)$$

Complete neutralisation is assumed within the membrane rather than an equilibrium forming. This is because any current carried by the reaction limiting species at equilibrium would be vanishingly small, and any small deviations from equilibrium are handled within the electrolyte domains through equation (18). However, it should be noted that for weak acids and bases this assumption is not sufficient. Through the combination of equations (30), 31, 37, and 38, the following relation for the effective current is derived:

$$i_{e,CEM} = \min\left\{ \frac{i}{1 - S_{OH,CEM}(1 - \bar{\bar{t}}_{CEM})} ; \frac{i}{1 - S_{H,CEM}\bar{\bar{t}}_{CEM}} \right\} \qquad (39)$$

$$i_{e,AEM} = \min\left\{ \frac{i}{1 - S_{H,AEM}(1 - \bar{\bar{t}}_{AEM})} ; \frac{i}{1 - S_{OH,CEM}\bar{\bar{t}}_{AEM}} \right\} \qquad (40)$$

In summary, using both a transport number and like-charge selectivity, the total flux, found from an effective current density, can be broken down first by charge identity (co-ion or counterion), and then into individual species. Finally, the membrane fluxes are summed for those adjacent to the appropriate channels and converted into concentration differentials using the flow velocity (u) and channel width (d).

$$\frac{dC_{i,j}}{dx} = \frac{1}{ud}\sum_m \alpha_{i,j,m}\left(J_{i,m} + \beta_{i,j,m,r}J_{r,m}\right) \qquad (41)$$

$$\alpha_{i,j,m} = \begin{cases} 1 & \text{if ion } i \text{ is transported though membrane } m \text{ into channel } j \\ -1 & \text{if ion } i \text{ is transported though membrane } m \text{ from channel } j \\ 0 & \text{if membrane } m \text{ is not adjacent to channel } j \end{cases} \qquad (42)$$

$$\beta_{i,j,m,r} = \begin{cases} -1 & \text{if ion } i \text{ is consumed in membrane } m \text{ and } \alpha_{i,j,m} \text{ is -1} \\ 1 & \text{if ion } i \text{ is produced in membrane } m \text{ and } \alpha_{i,j,m} \text{ is 1} \\ 0 & \text{otherwise} \end{cases} \qquad (43)$$

Here, the α factor ensures that the directionality of fluxes is accurately accounted for and only membranes adjacent to channel j are considered. The β factor ensures that reactions are correctly handled in the material balance; a consumed species transported through a membrane should leave with a flux equal to $J_{i,m}$, but arrive at a flux lower by $J_{r,m}$.

For an arrangement of n ionic species and m distinct channels, a system of $n \times m$ differential equations is required. In this work, this system was solved in MATLAB using the ode15s function, which utilises the Runge-Kutta method. The inlet concentrations were provided as boundary conditions from the outer layer, and the model returned the internal concentration profiles of each species in each channel. Other spatially dependent variables such as the total resistance, the fluxes of individual species over each membrane, the current density, and the cell voltage were also extracted.

2.3. Outer layer: Temporal material balance

The extension of the single-pass model (the middle layer) to that of a real system is crucial for model validation and experimental prediction. This is the function of the outer layer, which in this work involves modelling a recirculating batch system with different reservoirs for the acid, base, and diluate streams (Fig. 2a). The reservoirs are assumed well mixed and constant in volume. Assuming instantaneous fluid transfer, the temporal material balance for species i in reservoir j is as follows

$$\frac{dC_{R,i,j}}{dt} = -\frac{Q_j}{V_{R,j}}\left(C_{R,i,j}(t) - C_{i,j}(t, x = L)\right) \qquad (44)$$

Where $C_{R,i,j}$ is the concentration of species i in the reservoir of stream j, t is experimental time, Q is the recirculation volumetric flow rate, V_R is the reservoir volume, and $C_{i,j}(t, x = L)$ is the stack exit concentration.

Before this balance can be solved, $C_{R,i,j}$ is supplied to the middle layer as a boundary condition for the spatial material balance, from which $C_{i,j}(t, x = L)$ is returned.

The validity of this equation in light of the assumption of instantaneous fluid transfer is questionable as there is substantial dead time in the tubing and flow cells where measurements are taken. For the experimental setup in this work, the dead volumes were around 0.25 L for each stream, which is significant relative to the reservoir volume of 1 L. This dead-volume must be included in the parameter V_R to ensure that the overall material balance is accurate. Further, with a flow rate of 20 L/h, the time taken for the fluid to transfer from the reservoir to the stack and then back again is 45 s and thus not negligible. Consequently, the assumption of instantaneous fluid transfer between the reservoir and the stack may not be valid, and so a delayed differential equation is appropriate. Accounting for this delay, the material balance becomes

$$\frac{dC_{R,i,j}}{dt} = -\frac{Q_j}{V_{R,j}}\left(C_{R,i,j}(t) - C_{i,j}(t - \tau_j, L)\right) \qquad (45)$$

where the delay (τ_j) is the time for the flowing stream to complete a loop from the reservoir, through the stack, and return. Fluid leaving the reservoir is replaced by material which left a time τ ago, hence the form of this equation. It should be noted that consideration of a series of delays is necessary when comparing measured and computed variables whose domain is not the reservoir. The spatial difference results in a temporal variance, and so failure to account for this would result in a mismatch between data sets. Shifting all data to a relative 'standard time' is required. The MATLAB delayed differential equation solver dde23 was used in solving the temporal material balance.

3. Experimental validation

Modelling BPMED is notoriously complex due to the multitude of competing phenomena combining to influence overall mass transfer. Several assumptions were made in the development of this model to avoid reliance on training data and empirical fitting parameters. Consequently, the efficacy of this modelling strategy must be examined through experimental validation.

All experiments were performed on a PC BED 1–4 recirculating batch system (PC Cell) with an ED64004 stack (PC Cell). Here, three reservoirs are present, the fluids from which are circulated to the BPMED stack (Fig. 2a) The four membrane varieties used were the PC Acid 60 (AEM), PC MTE (CEM), PC Bip (BPM) and PC CE (eCEM), all from PC Cell. Eight full cell triplets were used rather than the typical ten to prevent an excessive voltage requirement. A Biologic SP300 potentiostat with 30 V/2A booster card was used to accurately control the applied stack potential and measure the current. The conductivity and pH of the three streams were measured close to either the stack inlet or outlet, depending on the experiment, using JUMO CTI-500 inline conductivity probes and JUMO digiLine pH sensors, respectively. Circulation flow rates were maintained at 20 L/h and reservoir volumes were accurately set at 1 L not including dead volume, which was determined independently.

To ensure model accuracy and robustness over a wide range of concentrations and voltages, experimental validation was conducted in two orthogonal ways:

1. **Temporal validation:** A typical batch experiment (Fig. 2a) was performed over the course of an hour with the voltage held constant at 20 V, and the pH, conductivity, and current measured at two second intervals. The pH and conductivity probes were positioned before the stack for each stream so that conditions were equal to that of the reservoir. The three reservoirs were filled initially with the same concentration of NaCl (0.05 M). Over time, the concentrations would diverge greatly, ensuring that a wide concentration range was

tested. A constant stream temperature of 20 °C was maintained by flowing chilled water through the reservoir jackets.

2. **Steady-state validation:** For this form of validation, current–voltage polarisation data was collected. The stack was operated in a continuous steady-state mode by flowing solution through only on a single pass. To achieve this, the outlets of each stream were not connected back to the reservoir, but instead to a waste collection container. The reservoirs which feed the pumps were topped up with fresh 0.05 M NaCl solution frequently to ensure that a constant inlet condition to the stack was maintained. An automatic chronoamperometry programme was set on the potentiostat software where the voltage was periodically stepped up by 1 V. A delay of 10——30 s between each step increase in the voltage ensured that any transitory current dissipated and a reasonable steady state was achieved.

For these orthogonal validation methods, model predictions were compared directly to experimental data. The same experimental characteristics and membrane parameters were used in both cases, presented in Table 1. All numerical values present here define the modelled system, but crucially were not used for any fitting. These parameters were either set through experimental practice, could be trivially measured, were known *a priori*, or could be found in manufacturer-provided data. As such, it is the model's predictive power that is being validated here.

3.1. Temporal validation

The evolution of solution conductivity at the stack inlet over time is seen in Fig. 4a. Here, experimental data is shown with points and model predictions with a solid line. At time zero, all three streams have the same conductivity (~5.9 mS/cm) in both the modelled and experimental data. Over time, the diluate conductivity decreases and the acid and base conductivities increase as Na^+ and Cl^- ions are transferred from the diluate to the base and acid streams, respectively. This continues until the diluate conductivity asymptotically approaches a very low value. At this point, the ions are nearly depleted in the diluate, and so the ion flux decreases and the acid and base conductivities level out.

The combined magnitude of the increase in the conductivities of the acid and base streams (~19 mS/cm and 10 mS/cm, respectively) is greater than the decrease in diluate conductivity (~5.9 mS/cm). This is

Table 1
Parameters and their associated values speficied in the model. also shown is how their value is obtained.

Parameter	Symbol	Value	Unit	Provenance
Applied Stack Voltage	V_{stack}	20	V	Set
Initial reservoir concentration	$C_R(t = 0)$	0.05	mol/L	Set
Reservoir volume	V_R	1.0	L	Set
Recirculation flowrate	Q	20	L/h	Set
Intermembrane distance	d	0.8	mm	Known system characteristic
Membrane area	A_m	64	cm²	Known system characteristic
Temperature	T	293	K	Measured system characteristic
Dead Volume	$V_{D,d}, V_{D,b}, V_{D,a}$	251, 248, 224	mL	Measured system characteristic
Time delay	τ_d, τ_b, τ_a	45, 45, 40	s	Measured system characteristic
Membrane thickness	d_m	0.1	mm	Manufacturer data
Membrane water fraction	f_w	0.22	–	Manufacturer data
Fixed charge concentration	C_{fix}	0.8	mol/L	Manufacturer data
Innate transport number	$\bar{t}_{0,cem} \bar{t}_{0,aem}$	0.99, 0.96	–	Manufacturer data

due to the water splitting reaction and generation of additional ions at the bipolar junction. Ideally, one transferred mole of NaCl forms a mole of NaOH and one mole of HCl. It can be seen through the Nernst-Einstein equation (equation (21) that contributions to the solution conductivity from each ion is proportional to both its concentration and diffusivity. The diffusivities of H^+ and OH^- ions are 9.31×10^{-9} m²/s and 5.27×10^{-9} m²/s, respectively; much higher than the 1.33×10^{-9} m²/s of Na^+ and 2.03×10^{-9} m²/s of Cl^-. Consequently, a solution of NaCl will have a lower conductivity than an equal concentration of NaOH or HCl. This also explains why the magnitude of the increase in the acid stream conductivity is greater than the increase in the base stream: The diffusivity of H^+ is greater than the diffusivity of OH^-.

The inlayed graph in Fig. 4a shows the system behaviour at the beginning of the experiment, just after the power supply has been switched on. An initial flat region in all conductivity trends can be seen which results from the time delay between fluid leaving the stack, returning to the reservoir, mixing, and then flowing out to the conductivity probe. This delay is represented in the model through a delayed differential equation and is crucial to capture early behaviour accurately.

The temporal evolution of the current density is shown in Fig. 4b. In both the experimental and model predicted data, there is an initial increase in the current density before it reaches a maximum at ~ 160 A/m² and then decreases. After passing an inflection point at ~ 760 s the current density asymptotically decreases to ~ 10 A/m². These trends in the current density can be explained through examining the contributions to the cell resistance from each of the three streams and investigating the evolution of the transport number. As discussed above, the increase in the conductivity of acid and base streams is faster than the decrease in the conductivity of the diluate stream. Since electrolyte resistance is inversely proportional to conductivity, the increase in the resistance of the diluate is initially offset by a larger decrease in the resistances of the acid and the base streams owing to the flood of additional ions. Consequently, the cell resistance decreases and the current density increases. However, the resistance of the diluate soon begins to dominate, again due to the inverse relationship to the conductivity, and the current density falls. As the diluate concentration falls to near-zero, the current, which is related to the gradient of the conductivity curve, would also be expected to fall to near-zero. The fact that it does not is notable and is discussed further below.

The residual current of ~ 10 A/m² at times greater than 3000 s is significant relative to the rate of change of the stream conductivities. In a model with a constant transport number, the rate of change of the reservoir concentration with time would be proportional to the current density. However, despite the gradient of the conductivity curves falling to 0.5 % of that at the start of the time series, the current only decreases to 5 % of the initial value. This can only be explained by a large reduction in the membrane transport numbers leading to unwanted back-migration and wasted current. This is exactly what is seen in the calculated transport numbers shown in Fig. 4c. Both membrane transport numbers are initially high at their intrinsic values but decrease to very low values. Additionally, the transport number for the AEM drops to a lower value than for the CEM. This explains the high current density relative to the overall mass transfer. As the concentration of ions in the acid and base streams increase to many times greater than that of the diluate, the rate of back-migration of co-ions increases. This is the dominant source of current across the AEM and CEM later in the experiment.

The transport number for the AEM drops lower than for the CEM because the AEM has a lower intrinsic transport number than the CEM. The overall transmembrane concentration ratios for both membranes remain similar throughout the experiment and thus the only difference in equation (32) is $\bar{t}_{m,o}$. Hence, the intrinsic transport number is the primary driver and so its value is crucial in establishing the membrane selectivity when extreme concentration gradients are present.

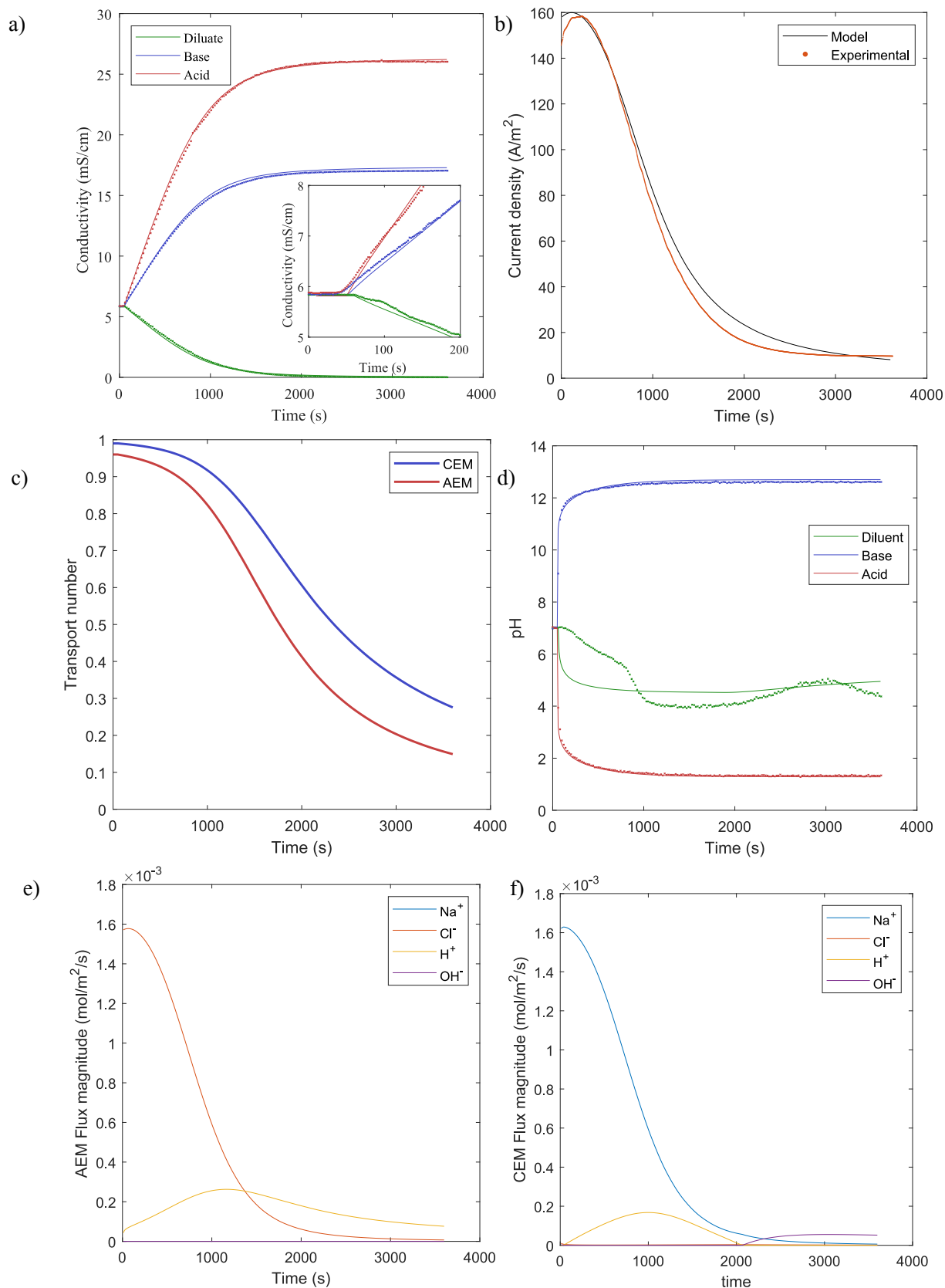When operating conventional ED, it is usually not possible for the

Fig. 4. Results of the temporal validation results. throughout, modelling results are shown with a solid line and experimental measurements are shown with points. a) the time-evolution of the conductivities of the three streams meausred/predicted at the reservoir outlet. the inlayed graph shows the behaviour early on. b) the meausred and calculated current density over time. c) the calculated transport numbers for the aem and cem over time. d) the time-evolution of the ph of all three streams, measures at the reservoir outlet. e) the calculated flux magnitude of all four species through the aem over time. f) the calculated time-evolution of the flux magnitude of all species through the cem.

average of the two transport numbers to fall below 0.5. A transport number of 0.5 means that equal amounts of current are carried by both co-ions and counterions. When this occurs in both membranes for conventional ED, there is no overall ion transport between the streams, and a stable equilibrium is reached. However, at a little after 2000 s in Fig. 4c, the average transport number for the AEM and CEM falls below 0.5 and towards the end reaches as low as 0.22. After this point, a majority of the current is being carried by co-ions from the acid and base streams into the diluate. Consequently, ~90 % of the 10 A/m^2 of current at the end of the experiment is involved in transporting protons and hydroxide ions from the BPM and across the AEM and CEM as co-ions, respectively, where they recombine. The energy expended in this cyclical process splitting and recombining water molecules is entirely lost.

The flux magnitudes of each ion across the CEM and AEM are shown in Fig. 4e and f, respectively. Current is transported through the AEM by Cl$^-$ and H$^+$ and through the CEM by Na$^+$, OH$^-$, and H$^+$ ions. The effect of the low transport numbers can very clearly be seen here. The trends of the Na$^+$ and Cl$^-$ fluxes across the CEM and AEM, respectively, follow a very close trend to the current, with one key difference. They initially increase before decreasing to an inflection point and asymptotically approach a low value. However, while the fluxes of Na$^+$ and Cl$^-$ approach a flux of zero as ions are depleted in the diluate, the current does not. Proton and hydroxide co-ion transport from the acid and base to the diluate begins to dominate at later times, again demonstrating that the current flowing is being wasted on water splitting followed by recombination. An interesting difference between Fig. 4e and f is that while proton co-ion flux is present within the AEM for the entire duration, the same is not true about hydroxide ions and the CEM. This will be explored further in section 4.2.

The evolution of the predicted and experimentally measured pH is shown in Fig. 4d. All three streams start off at a pH of around 7, as expected for a neutral NaCl solution. Soon after the power supply is activated, the pH of the base rapidly increases, and the pH of the acid rapidly decreases, in line with the model results and what would be expected. However, there is a clear difference between the experimental and modelling results for the pH of the diluate stream. The diluate pH decreases slowly relative to what is predicted, before dropping faster and steadily rising again. Several inflection points can be seen in the experimental data which is not present in the model predictions. This trend was seen qualitatively in all experimental repeats performed but differed somewhat quantitatively. The change in the diluate pH is the result of protons and hydroxide ions permeating as co-ions from the acid and base streams, respectively. Hence, if an ideal membrane permselectivity is assumed, the diluate pH would remain more-or-less constant. The flux of protons and hydroxide ions depends very strongly on several parameters which change significantly over the course of the experiment. These are the current density, membrane transport number, and like-charge selectivity. Extreme differences in concentrations across the membranes are present almost immediately, affecting the like-charge selectivities strongly. Further, since pH is a logarithmic function, small changes in the concentration have disproportionate effects on the pH for neutral solutions. Since the diluate pH remains around 5 to 7 and is adjacent to the acid and base streams with concentrations many orders of magnitudes higher, there are likely to be small degrees of ion crossover not accounted for which result in pH fluctuations. Consequently, the fluctuating nature of the pH of the diluate and the lack of predictability is not unexpected.

An implicit model assumption which might also contribute to the poor prediction of the diluate pH is that of instantaneous transfer or the 'hopping' of ions between the bulk mixed regions of the different streams. This is an artifact resulting from how concentrations are handled by the model. For a given differential slice of the stack (position), it is assumed that the ion flux leaving one channel through a given membrane is equal to the flux entering the corresponding channel adjacent to the same membrane. In other words, there is no accumulation inside the membrane, implying steady-state behaviour or that ions 'hop' between channels. Consequently, protons produced within the BPM can be transported from the BPM to the bulk of the acid stream, then across the AEM, diluate, and CEM to the base channel, effectively instantaneously. For a system operating close to steady state, where changes to the inlet concentration happen slowly, this is a reasonable assumption. However, the pH can be seen to change very rapidly in all three streams. If the real time taken for ions to cross the membranes and boundary layers is of a similar or greater order of magnitude to changes to the inlet conditions, the transit time will have a large effect.

The permeation transit time (t_p) for a membrane can be estimated *via* a permeation superficial velocity (flux divided by membrane concentration), along with the membrane thickness and water (void) fraction:

$$t_{p,m} = \frac{d_m f_w C_m}{J_m} \tag{46}$$

For dilute electrolytes, the membrane concentration (C_m) is approximately equal to the fixed charge concentration according to the Donnan equilibrium. Hence, t_p is ~ 60 s for both membranes. This is very significant compared to the residence time of the flow within each channel at ~ 4 s and for the changes in inlet conditions to the base and acid streams. Sixty seconds after the stream inlets begin to change, the base and acid have a pH of 11.5 and 2.5, respectively. For a change this drastic, the permeation transit time is significant and thus could be responsible for the sluggish change in the experimentally observed diluate pH. Nevertheless, industrial operations of BPMED will operate a continuous process where long-term changes do not manifest. As such, the overall impact of the poor predictability of the diluate pH is minimal.

To quantify the agreement between the model prediction and experimental data, the average absolute difference (AAD) for each data series was calculated.

$$\text{AAD} = \frac{1}{N_o}\sum\nolimits_{o=\text{observation}} |\chi_o - \overline{\chi}_o| \tag{47}$$

Here, N_o is the total number of data points recorded, χ_o is an experimentally observed data point at a particular time, and $\overline{\chi}_o$ is the associated model prediction for the same point in time. Table 2 shows the calculated values of the AAD for each data series along with their initial values to aid comparison. For almost all variables, the AAD is less than 2 % of the initial value, demonstrating strong agreement between model predictions and experimental results. The diluate pH is the exception to this, the reasons for which have been explained above. The AAD values in this work are slightly larger than those for conventional ED presented in previous work, but not markedly so. This is somewhat expected due to the much greater complexity of BPMED and the incorporation of additional phenomena, each of which contributes a potential source of error. Nevertheless, the low AAD values demonstrates the accuracy of the model despite the lack of experimental fitting parameters and training data.

For both the conductivity and current density, there is very good

Table 2
A table evaluating the goodness of fit of the model to experimental data, as represented by the average absolute difference (AAD) and calculated using equation (47). The value of the variable at the start of the experiment is shown to aid comparison.

Measured Variable	AAD	Initial Value
Current Density	4.51 A/m^2	157 A/m^2
Diluate Conductivity	0.097 mS/cm	5.95 mS/cm
Base Conductivity	0.187 mS/cm	5.95 mS/cm
Acid Conductivity	0.158 mS/cm	5.95 mS/cm
Diluate pH	0.56	7.0
Base pH	0.09	7.0
Acid pH	0.06	7.0

agreement between model predictions and experimental results. Both qualitative and quantitative agreement is seen throughout the entire time of the experiment. Further, the fact that the mass balance is met for all three streams gives confidence to model accuracy. This would not be possible without a model for how the transport numbers evolve, as they can be seen to fall by nearly an order of magnitude. A fixed transport number would result in a significant mismatch between experimental results and model predictions. Taking a high fixed transport number would mean under-predicting the current at the end of the experiment and choosing a low fixed transport number would result in the rate of change of the stream conductivities being too slow.

The assumption of negligible diffusion can be scrutinised here. Ion diffusion is greatest relative to electromigration towards the end of the experiment when the transmembrane concentration difference is greatest. The maximum concentration difference attainable is on the order of 100 mol/m^3. With a membrane diffusivity of $\sim 1 \times 10^{-11}$ m^2/s and membrane thickness of 0.5 mm, this gives a membrane diffusion flux of 2×10^{-6} mol/m^2/s. At the end of the experiment, the current density is ~ 10 A/m^2. Dividing this by the Faraday constant gives an electromigratory flux of $\sim 1 \times 10^{-4}$ mol/m^2/s. This is two orders of magnitude greater than the diffusion flux. It should be noted that under these circumstances, the rate of diffusion is greatest relative to electromigration. Thus, the assumption that transport by diffusion is negligible relative to electromigration is justified.

3.2. Steady-state current–voltage validation

Current-voltage polarisation curves are ubiquitous in the research of electromembrane systems. As such, the ability to accurately model this behaviour is paramount for design and optimisation. When operating an electromembrane unit there is an inherent trade-off between the specific energy consumption and total membrane area, which comprise a large proportion of the operating and capital costs, respectively. The specific energy consumption is proportional to the applied voltage, and the membrane area is inversely proportional to it. Therefore, an optimum voltage and membrane area exists which minimises the total costs of a BPMED operation. Accurate process design and optimisation of units is one of the objectives of this modelling work, and so this form of validation is essential.

Fig. 5a shows the time series data for the applied voltage and measured current density. After each step increase in the voltage, the current can be seen to spike, before asymptotically decreasing towards a new steady state. This occurs because there is an initial surge of current resulting from the transient thickening of the electric double layer and an increase in the degree of concentration polarisation as a new equilibrium concentration field develops. Additional current resulting from these effects would not be present during steady-state operation, and so is allowed to dissipate before the measurement is taken. The time taken to reach a new equilibrium is demonstrative that transport is far from instantaneous, providing evidence for the claim that this delays changes to the diluate pH. There is much less transient behaviour above 10 V, where the current reaches its steady-state value almost immediately.

Fig. 5b shows the resulting steady-state current–voltage response curve for both the experimental data and model predictions. At low voltages, below ~ 5 V, there is essentially no steady-state current seen in either the model or experimental data. This is because there is a minimum operating voltage for current to flow, which results from the reactions that occur within the bipolar membrane and at the electrodes. The electrode reactions have an equilibrium potential of 1.23 V, and the bipolar junction potential drop is proportional to the pH difference across it (equation (12). Any meaningful current immediately results in a value of ΔpH on the order of 10, and so an effective minimum bipolar potential drop can be calculated to be ~ 0.5 V. Summing these voltage drops for the eight bipolar membranes and the electrode reactions shows that for any current to flow, a minimum voltage of 5.23 V is required.
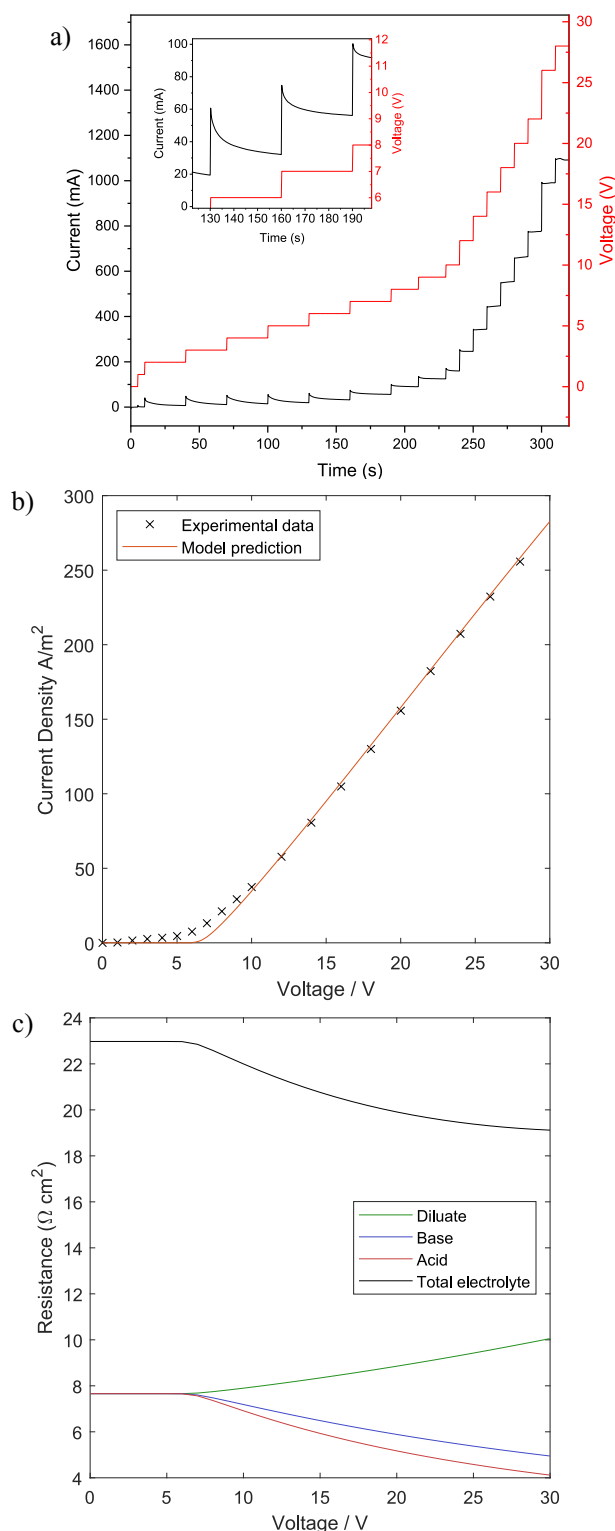

Fig. 5. Results of the steady-state validation. a) The temporal profile of the current (black) and voltage (red) over the course of the experiment. The inlayed graph shows a magnified area highlighting the assymptotic approach to a steady state. b) The steady state current–voltage response curve. Experimental measurements are shown with crosses and the model is shown with a solid line. c) A graph showing how the calculated resistances for the three streams and the total electrolyte resistance vary with the applied voltage. (For interpretation of the references to colour in this figure legend, the reader is referred to the web version of this article.)

This is reflected in both the model and experimental results.

At higher voltages, above 10 V, the current–voltage response appears to be linear, characteristic of a constant resistance. As voltage increases, the electrolyte resistance is the only resistive element which meaningfully changes. The membrane resistance, bipolar junction potential drop and electrode overpotential do all change as well, but by a relatively low amount due to the form of their equations. The electrode overpotential is a logarithmic function of the current density, whereas the BPM voltage drop, and membrane resistance are both affected by the internal ion concentration. For the dilute solutions used in these experiments, the internal concentration is close to the membrane fixed charge density and does not vary much with the external solution. However, the electrolyte resistances are more directly affected by the applied voltage. A higher voltage will result in a decrease in the diluate concentration and an increase in the acid and base concentrations due to greater salt transfer and water splitting. Resultantly, increasing the voltage increases the diluate resistance and reduces the acid and base resistances (Fig. 5c). The increase in the resistance of the diluate is greater than the decrease in acid and base resistance since they are inversely proportional to the salt concentration. However, the additional H^+ and OH^- ions to the acid and base streams from the BPM offsets this difference, resulting in a small overall reduction in the total electrolyte resistance. This is the same effect that causes the current density to initially increase in the early stages of the temporal validation experiments (Fig. 4b). Even so, the overall impact to stream concentrations is relatively low over this voltage range as the inlet concentrations are constant. Consequently, the overall resistance of the stack in the voltage range only slightly increases and so a near-linear trend in the current–voltage curve is seen.

There is a very good agreement between the model prediction and experimental current–voltage polarisation data, with an AAD of 3.11 A/m^2. This is very low compared to the range of current density that is measured (250 A/m^2), demonstrating the close match between the model and the data. The largest divergence occurs during the transition above the minimum splitting voltage around 5 V. Here, experimentally measured currents are somewhat larger than those predicted by the model. One potential reason could be that not enough time was allowed for the transitory current to dissipate after each step-increase in the voltage. The decay of this current was slowest within the transition region, and thus it would have the greatest effect here. This can be evidenced by the tails of the current in Fig. 5a do not quite reach a steady value. Alternately, the assumption of the exclusion of external ions from the BPM could be responsible. Small amounts of Na^+ and Cl^- ions permeating the BPM at low voltages could provide the low amount of current seen. Nevertheless, the close agreement between the experimental data and model predictions for the current–voltage polarisation curves demonstrates that the model is accurate over a wide range of voltages.

4. Model exploration

There are a huge number of individual phenomena comprising BPMED which all aggregate and influence the macroscale variables that are experimentally measured. A core strength of mathematically modelling complex processes is the ability to extract the profiles of the variables representing those phenomena. This is particularly useful for BPMED and other electromembrane processes where empirical measurement of some phenomena is unfeasible. Understanding which phenomena are limiting allows for conclusions to be drawn about where future research developments can have the greatest benefit. For BPMED, acid-base reactions are one of the most obfuscated phenomena which also has a huge impact on the overall process. In this section, the numerically predicted reaction trends are explored.

Another valuable insight to be gained through model analysis is the impact of the assumptions made during development. Thes can be readily evaluated by directly comparing data from predictions where the assumption is active and inactive. Here, the impacts of using a delayed

temporal material balance and an effective current density are assessed to evaluate their underlying assumptions.

4.1. The impact of a delayed temporal balance

The inclusion of a delayed temporal material balance was determined to be necessary to account for the significant time taken for the fluid to be transferred from the reservoirs to the stack and back again. Here, the impact of the inclusion of this delay is investigated. The model prediction curves used for experimental validation in section 3.1 for the conductivity and current density are presented in Fig. 6a and b, respectively. The only difference between the models used to generate the two curves is whether a time delay has been included in the material balance. There is a clear difference between the two predicted trends, where changes in measured variables in the non-delayed predictions occur earlier and faster. The difference cannot be completely removed by simply shifting the predicted data series to a later time. If experimental fitting on training data was used to attempt to match the non-delay predictions to the experimental results (which closely match the delay predictions), then erroneous manipulations would occur. The ion flux would need to be reduced to artificially slow down changes to conductivities while maintaining a similar current density. This could potentially involve artificially reducing the membrane transport numbers, lowering the efficiency and slowing down overall changes. Consequently, the extrapolation of the fitted model to a different system would be greatly hampered.

A further impact of including a delay can be seen in a clear difference between the asymptotic limits that the acid conductivity reaches after 2000 s. This is likely due to the delay measured for the acid stream being 5 s lower than for the other two streams. This slight difference on a single pass accumulates over the duration of the experiment producing a meaningful difference. Again, removing this effect by fitting the model to training data would be possible but reduces the model's globality.

4.2. Investigating the rate of reactions

The temporal profile for the overall rate of water-recombination reactions in each of the five reacting domains is shown in Fig. 7a. This data has been extracted from the predicted profiles generated for the experimental validation of section 3.1. Here, the water recombination reaction where H^+ and OH^- ions form water is defined as positive, and the reverse as negative. The reaction rate is always positive, indicating that the recombination reaction is dominant over splitting. This makes intuitive sense, since the ions produced in the bipolar membrane are an excess to the equilibrium already present. Therefore, it is the recombination reaction that is consistently the direction taken back to that equilibrium.

The total rate of reaction can be seen to increase initially before peaking and then decreasing, before reaching a second, sharp peak, at just after 2000 s. This overall profile is the sum of trends in three of the five domains, where the reaction sequentially dominates. Reaction is fastest first in the base stream before the CEM takes over, and then within the diluate, this time tending towards a stable value. The current density is a key driver of the overall reaction trend witnessed (Fig. 4b). A higher current density results in a greater rate of water splitting in the BPM, a higher migratory flux of protons and hydroxide ions, and thus a greater rate of reaction. However, the rate of reaction peaks at about 1200 s, long after current density does at 120 s. This is because most of the reaction occurs between protons and hydroxide ions that have leaked through the AEM and CEM as co-ions, respectively. As such, the rate of co-ion migration is the greatest driver of the reaction rate. The increasing concentration in the acid and base streams and declining concentration of the diluate stream both reduces the transport number of the membranes and increases the like-charge selectivity to protons and hydroxide ions. Both these effects combine to increase the flux of H^+ and OH^- through the AEM and CEM, respectively, even as the current
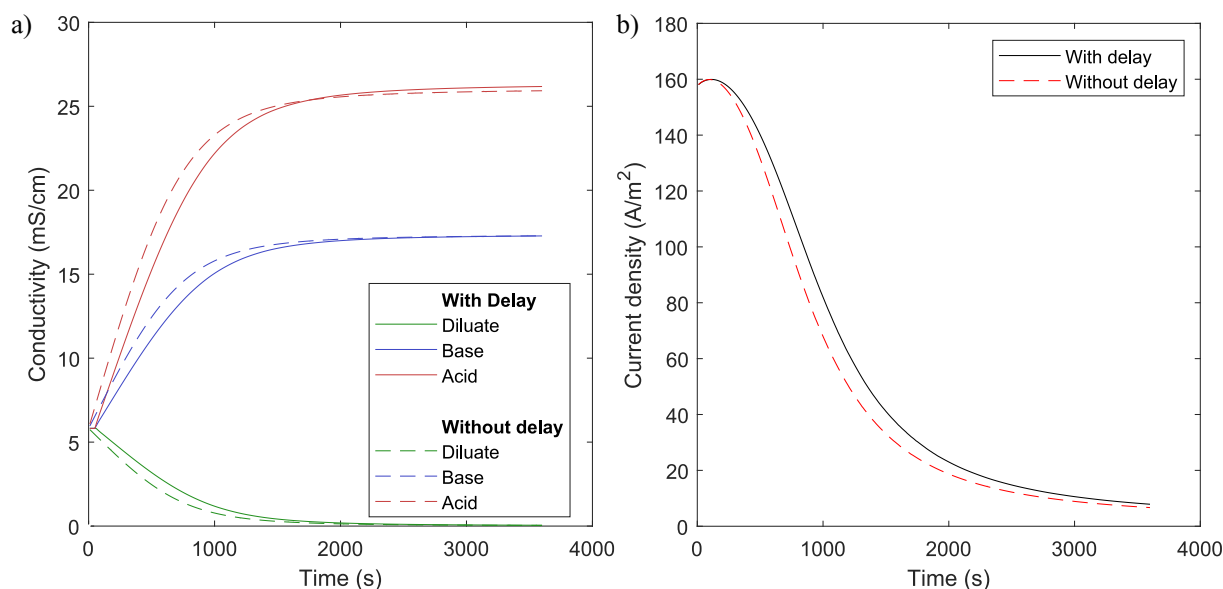
Fig. 6. An evaluation of the effect of a time-delayed material balance. a) a comparison of the evolution of the calculated conductivity with and without the inclusion of a delay in the material balance. b) A graph showing the effect the inclusion of a delay has on the current density.
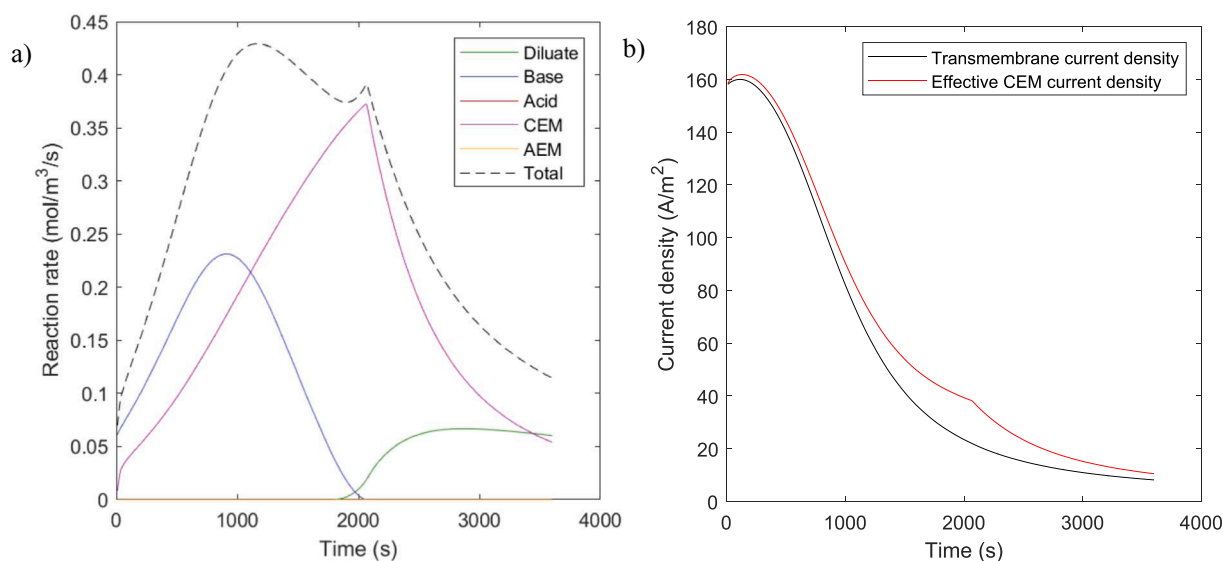

Fig. 7. A) a graph showing the temporal evolution of the rate of reaction within each of the five domains (three streams, two membranes) where the water recombination reaction is defined as positive. the total reaction rate is shown with a dashed line. b) a comparison of the calculated effective current density and the 'true' or transmembrane current density.

density is decreasing.

The observed successive dominance of reaction within the base, CEM, and diluate is indicative of a shifting reaction plane. The lower intrinsic transport number of the AEM relative to the CEM (0.96 to 0.99) and the higher diffusivity of protons results in the co-ion flux of protons to the diluate from the acid being initially around six times that of hydroxide ions from the base. This is illustrated by the drop in the pH of the diluate. Subsequent transport of protons across the CEM to the base stream is fast since they are now transported as counterions and hence overwhelm hydroxide co-ion transport. Consequently, the reaction is initially dominant within the base stream. Over time as the diluate concentration decreases, the transport numbers of both the transporting membranes decrease. The decreasing CEM transport number along with the increasing like-charge selectivity to hydroxide ions result in the co-ion flux of OH^- increasing and thus the reaction plane shifts to within the CEM. The peak of the CEM reaction rate at just after 2000 s coincides

with when the hydroxide flux matches and then exceeds the proton flux (Fig. 4f). At the peak, the fluxes of protons and hydroxide ions are equal, leading to complete neutralisation and no transmembrane migration of these ions. After this point, the flux of hydroxide ions exceeds that of protons in the CEM, shifting the reaction plane to within the bulk of the diluate. The sharp peak present in the CEM reaction rate is the result of how the reaction flux is calculated in equation (37): it is the lower of the H^+ and OH^- fluxes. Since they intersect at a point when hydroxide flux is increasing and proton flux is decreasing, a smooth function is not expected. The approach to a steady current density and rate of reaction in the diluate towards the end of the time series suggests that at this point, a stable situation is arising. Here, protons and hydroxide ions are generated within the BPM and are ultimately both transported to the diluate where they combine once again, wasting energy.

Negligible reaction can be seen in the AEM and the acid streams which results from the transport number of the AEM being lower than

the CEM. Hydroxide ions do not get a chance to make it to the acid stream before being neutralised either in the CEM or the diluate. As such, the only reaction in the acid stream is the negligible buffering effect that the existing hydroxide ions have (mostly constant at $\sim 2.7 \times 10^{-3}$ mol/m^3/s).

Through these results, a weakness of the circuit-based modelling strategy can be seen. Modelling using the Nernst-Planck equation in software such as COMSOL Multiphysics reveals that due to the rapid kinetics, water recombination reactions essentially occur within a plane. However, in Fig. 7a, a considerable amount of reaction is occurring concurrently in multiple domains. This results from two features of the circuit-based model: plug flow within the channels (one-dimensional concentration profiles) and instantaneous transfer between the domains. During the early stages of the time series, proton transfer is greater than hydroxide transfer over the CEM, but both are significant, so there is substantial reaction within the CEM. However, because transport is instantaneous and the bulk electrolytes are assumed to be well mixed, the excess protons transported over the CEM then react with the large hydroxide concentration within the base stream. In reality, a reaction plane would be formed, most likely within the CEM or the boundary layer of the base stream.

Despite this inaccuracy, there is no impact on the overall model predictions which would affect process design and optimisation. The overall rate of recombination, in mol/s, is about four orders of magnitude lower than the ion molar flow of the streams passing through the stack. Therefore, while accounting for reactions is important for a long duration experiment, the precise location of where these reactions occur is not. Further, an estimate for the location of the 'true' reaction plane can be discerned from the relative reaction rates in the base, CEM, and diluate domains. It is likely to exist somewhere between the two active domains and depend on their relative rates. Flow boundary layers are not considered within this model but are a likely place for reactions to occur. Again, simply accounting for this excess of ions within the model is sufficient for macro-scale results to be accurate. Deeper insight into the precise location of the reaction plane may be hampered, but the success in achieving the original goal of the model is not affected.

The effect that considering membrane reactions and an effective current density has can be seen in Fig. 7b, where the effective current density of the CEM is compared to the 'true' current density. The effective current density of the CEM is always greater than the actual transmembrane current density due to the acid-base reactions occurring. The difference between the two curves increases and peaks at just after 2000 s when the rate of reaction within the CEM is the greatest. At this point, the effective current density is ~ 75 % higher than the transmembrane current density. As such, there is a proportional increase in the flux of all ions across the CEM, including sodium and chloride ions. Failure to account for this would result in an inaccurate prediction of the flux. For the set of conditions present in this work, the impact would be limited since the change in the stream conductivities after 2000 s is very low (Fig. 4a). However, for a different application with a more concentrated feed, this could be very significant.

5. Conclusion

In this work, the development, validation, and exploration of a novel circuit-based process model of BPMED is presented. This model was developed without the use of training data or empirical fitting parameters, instead relying on manufacturer provided data only. Consequently, it is hoped that the globality of the model is greatly improved. The model basis uses the analogy of an electric circuit, with different resistive elements for each of the membranes and electrolyte streams. Further, the model was segmented into three layers based on the scale of the domain they consider. In the innermost layer, the current density is

found by applying Ohm's law to a differential slice of a cell pair from a cell voltage and cell resistance. The current density was used within the middle layer along with a transport number and like-charge selectivity to compute the fluxes of all species across all membranes using Faraday's first law. This could then be converted to a concentration differential using a spatial material balance and integrated to generate an internal concentration profile. Acid-base reactions were also considered, and assumed to be fast enough that active species were always at equilibrium. Their effect within the membranes of releasing additional current was also captured through the computation of an 'effective' current density. The outlet layer considers adaption to a real process that the stack is a part of, which in this work was a recirculating batch experiment. A delayed temporal material balance was used to compute how the concentration of each species in each reservoir varies with time while accounting for the pipe dead-time encountered by each stream.

Experimental validation of the model was conducted in two orthogonal ways. The first method involved a standard recirculating batch experiment with a fixed voltage and comparing experimentally measured variables (current density, conductivity, and pH) with model predictions. A sub-model which computes the transport number in of each membrane proved vital for accurately computing how the selectivity of each membrane varies. Computed transport numbers fell from near unity to below 0.3, confirming that the use of a fixed transport number is not sufficient. In the second experimental validation, a series of steady-state currents were measured for a range of applied voltages, this time maintaining a constant inlet concentration. Transient currents present after each step-increase in the voltage were allowed to subside and the final steady-state current was compared to model predictions. Both validation methods showed excellent agreement despite the lack of parameter fitting, demonstrating that the model is valid over a wide range of concentrations and voltages.

The use of a delayed temporal material balance to account for pipe dead time is not typical in existing models but was shown here to have a large impact on the temporal evolution of important variables. Small differences were shown to aggregate over lengthy experimental periods and have significant outcomes, especially when streams have different time delays. Further, experimental fitting of a non-delayed model would result in erroneous predictions of important variables such as the electrical resistance or the transport number.

Analysis into the model predictions and calculated fluxes revealed that proton leakage over the AEM is a significant contributor to process inefficiency. Significant proton co-ion flux across the AEM was present throughout the experiment and by the end it was by far the dominating source of current across the membrane. This indicates a strong need to develop AEMs with a higher permselectivity to inhibit the transfer of protons relative to anionic counterions and increase process efficiency.

An exploration of the relative reaction rates for water recombination between the three streams revealed a model limitation where reactions are predicted to occur in multiple streams, rather than in a plane. This limitation arises from the assumptions of instantaneous transfer or ion hopping across membranes and plug flow within the channels. Despite this, it was determined this would have a low overall effect on the model's predictive power for the key variables. Further, the relative reaction rates in each stream could be used to discern an estimated location of the reaction plane within the unit cell.

The primary limitation of this model is that it has only been tested on a single case-study using NaCl as the electrolytic feedstock. This simple case was chosen to ensure that the fundamental phenomena driving BPMED were accurately captured. Future work should focus on expanding the application of the model to more commercially relevant scenarios.

Overall, the flexibility and lack of reliance on fitting to training data are core strengths of the model which can be built on to further improve

its predictive capabilities. As BPMED systems become more commercially viable, models such as the one presented herein will prove to be powerful tools for both researchers and industry.

CRediT authorship contribution statement

Jack Ledingham: Writing – review & editing, Writing – original draft, Visualization, Validation, Software, Methodology, Investigation, Formal analysis, Data curation, Conceptualization. **Kyra L. Sedransk Campbell:** Writing – review & editing, Supervision, Funding acquisition, Conceptualization. **Ben in 't Veen:** Writing – review & editing, Supervision, Funding acquisition. **Lucas Keyzer:** Writing – review & editing, Supervision, Funding acquisition. **Ngai Yin Yip:** Writing – review & editing, Supervision. **Alasdair N. Campbell:** Writing – review & editing, Visualization, Supervision, Methodology, Conceptualization.

Declaration of competing interest

The authors declare that they have no known competing financial interests or personal relationships that could have appeared to influence the work reported in this paper.

Data availability

Data will be made available on request.

Appendix A. Supplementary data

Supplementary data to this article can be found online at https://doi.org/10.1016/j.cej.2024.154895.

References

[1] I. Renewable Energy Agency, Renewable Power Generation Costs in 2022, (2023). www.irena.org (accessed January 23, 2024).

[2] IEA, World Energy Balances, (2019). https://www.iea.org/reports/world-energy-balances-overview/world (accessed January 23, 2024).

[3] O. Edenhofer, Y. Sokona, J.C. Minx, E. Farahani, S. Kadner, K. Seyboth, A. Adler, I. Baum, S. Brunner, B. Kriemann, J. Savolainen Web Manager Steffen Schlömer C. von Stechow, T. Zwickel Senior Scientist, Climate Change 2014 Mitigation of Climate Change Working Group III Contribution to the Fifth Assessment Report of the Intergovernmental Panel on Climate Change Edited by, (2014). www.cambridge.org (accessed January 23, 2024).

[4] M. Wei, C.A. McMillan, S. de la Rue du Can, Electrification of Industry: Potential, Challenges and Outlook, Current Sustainable/Renewable Energy Reports 6 (2019) 140–148. https://doi.org/10.1007/S40518-019-00136-1/TABLES/1.

[5] J. Deason, M. Wei, G. Leventis, S. Smith, L. Schwartz, Electrification of buildings and industry in the United States Drivers, barriers, prospects, and policy approaches, (2018).

[6] R. Pärnamäe, S. Mareev, V. Nikonenko, S. Melnikov, N. Sheldeshov, V. Zabolotskii, H.V.M. Hamelers, M. Tedesco, Bipolar membranes: A review on principles, latest developments, and applications, J Memb Sci 617 (2021) 118538, https://doi.org/10.1016/J.MEMSCI.2020.118538.

[7] L. Chen, Q. Xu, S.Z. Oener, K. Fabrizio, S.W. Boettcher, Design principles for water dissociation catalysts in high-performance bipolar membranes, Nature Communications 2022 13:1 13 (2022) 1–10. https://doi.org/10.1038/s41467-022-31429-7.

[8] T. Chen, J. Bi, Z. Ji, J. Yuan, Y. Zhao, Application of bipolar membrane electrodialysis for simultaneous recovery of high-value acid/alkali from saline wastewater: An in-depth review, Water Res 226 (2022) 119274, https://doi.org/10.1016/j.watres.2022.119274.

[9] J. Xu, G. Zhong, M. Li, D. Zhao, Y. Sun, X. Hu, J. Sun, X. Li, W. Zhu, M. Li, Z. Zhang, Y. Zhang, L. Zhao, C. Zheng, X. Sun, Review on electrochemical carbon dioxide capture and transformation with bipolar membranes, Chinese Chemical Letters 34 (2023) 108075, https://doi.org/10.1016/J.CCLET.2022.108075.

[10] Y. Zhang, Z. Zhang, K. Guo, X. Liang, Controllable recovery and recycling of carboxylic acid-polyalcohol deep eutectic solvent for biomass pretreatment with electronically-controlled chemical methodology, Bioresour Technol 365 (2022) 128175, https://doi.org/10.1016/J.BIORTECH.2022.128175.

[11] Y. Liu, M. Lv, X. Wu, J. Ding, L. Dai, H. Xue, X. Ye, R. Chen, R. Ding, J. Liu, B. Van der Bruggen, Recovery of copper from electroplating sludge using integrated bipolar membrane electrodialysis and electrodeposition, J Colloid Interface Sci 642 (2023) 29–40, https://doi.org/10.1016/J.JCIS.2023.03.154.

[12] C. Huang, T. Xu, Electrodialysis with bipolar membranes for sustainable development, Environ Sci Technol 40 (2006) 5233–5243, https://doi.org/10.1021/ES060039P/ASSET/IMAGES/LARGE/ES060039PF00008.JPEG.

[13] S.K. Patel, B. Lee, P. Westerhoff, M. Elimelech, The potential of electrodialysis as a cost-effective alternative to reverse osmosis for brackish water desalination, Water Res 250 (2024) 121009, https://doi.org/10.1016/J.WATRES.2023.121009.

[14] A. Culcasi, L. Gurreri, A. Cipollina, A. Tamburini, G. Micale, A comprehensive multi-scale model for bipolar membrane electrodialysis (BMED), Chemical Engineering Journal 437 (2022) 135317, https://doi.org/10.1016/J.CEJ.2022.135317.

[15] J.L. Gineste, G. Pourcelly, Y. Lorrain, F. Persin, C. Gavach, Analysis of factors limiting the use of bipolar membranes: a simplified model to determine trends, J Memb Sci 112 (1996) 199–208, https://doi.org/10.1016/0376-7388(95)00284-7.

[16] S. Koter, A. Warszawski, A new model for characterization of bipolar membrane electrodialysis of brine, Desalination 198 (2006) 111–123, https://doi.org/10.1016/J.DESAL.2006.09.016.

[17] M.P. Mier, R. Ibañez, I. Ortiz, Influence of ion concentration on the kinetics of electrodialysis with bipolar membranes, Sep Purif Technol 59 (2008) 197–205, https://doi.org/10.1016/J.SEPPUR.2007.06.015.

[18] E. Vera, J. Sandeaux, F. Persin, G. Pourcelly, M. Dornier, J. Ruales, Modeling of clarified tropical fruit juice deacidification by electrodialysis, J Memb Sci 326 (2009) 472–483, https://doi.org/10.1016/J.MEMSCI.2008.10.034.

[19] L. Shi, Y. Hu, S. Xie, G. Wu, Z. Hu, X. Zhan, Recovery of nutrients and volatile fatty acids from pig manure hydrolysate using two-stage bipolar membrane electrodialysis, Chemical Engineering Journal 334 (2018) 134–142, https://doi.org/10.1016/J.CEJ.2017.10.010.

[20] S.S. Melnikov, O.A. Mugtamov, V.I. Zabolotsky, Study of electrodialysis concentration process of inorganic acids and salts for the two-stage conversion of salts into acids utilizing bipolar electrodialysis, Sep Purif Technol 235 (2020) 116198, https://doi.org/10.1016/J.SEPPUR.2019.116198.

[21] F. Scholz, Books on Fundamental Electrochemistry and Electroanalytical Techniques, Electroanalytical Methods (2010) 343–345, https://doi.org/10.1007/978-3-642-02915-8_19.

[22] S. Mafé, P. Ramírez, A. Alcaraz, Electric field-assisted proton transfer and water dissociation at the junction of a fixed-charge bipolar membrane, Chem Phys Lett 294 (1998) 406–412, https://doi.org/10.1016/S0009-2614(98)00877-X.

[23] J. Schiffbauer, N.Y. Ganchenko, G.S. Ganchenko, E.A. Demekhin, Overlimiting current due to electro-diffusive amplification of the second Wien effect at a cation-anion bipolar membrane junction, Biomicrofluidics 12 (2018), https://doi.org/10.1063/1.5066195/133883.

[24] A. Ortega, L.F. Arenas, J.J.H. Pijpers, D.L. Vicencio, J.C. Martínez, F.A. Rodríguez, E.P. Rivero, Modelling water dissociation, acid-base neutralization and ion transport in bipolar membranes for acid-base flow batteries, J Memb Sci 641 (2022) 119899, https://doi.org/10.1016/J.MEMSCI.2021.119899.

[25] T. León, J. López, R. Torres, J. Grau, L. Jofre, J.L. Cortina, Describing ion transport and water splitting in an electrodialysis stack with bipolar membranes by a 2-D model: Experimental validation, J Memb Sci 660 (2022) 120835, https://doi.org/10.1016/J.MEMSCI.2022.120835.

[26] Y. Wang, A. Wang, X. Zhang, T. Xu, Simulation of electrodialysis with bipolar membranes: Estimation of process performance and energy consumption, Ind Eng Chem Res 50 (2011) 13911–13921, https://doi.org/10.1021/IE200467S/ASSET/IMAGES/LARGE/IE-2011-00467S_0008.JPEG.

[27] C. Jiang, S. Li, D. Zhang, Z. Yang, D. Yu, X. Chen, Y. Wang, T. Xu, Mathematical modelling and experimental investigation of CO2 absorber recovery using an electro-acidification method, Chemical Engineering Journal 360 (2019) 654–664, https://doi.org/10.1016/J.CEJ.2018.12.006.

[28] S. Koter, Modeling of weak acid production by the EDB method, Sep Purif Technol 57 (2007) 406–412, https://doi.org/10.1016/J.SEPPUR.2006.03.005.

[29] J. Ledingham, K.L. Sedransk Campbell, B. in 't Veen, L. Keyzer, N.Y. Yip, A.N. Campbell, The development and validation of a novel, parameter-free, modelling strategy for electromembrane processes: Electrodialysis, Desalination 576 (2024) 117386. https://doi.org/10.1016/J.DESAL.2024.117386.

[30] G.S. Ohm, Die galvanische Kette, Bei T.H. Riemann, 1827. https://doi.org/10.5479/sil.354716.39088005838644.

[31] J. Tafel, Über die Polarisation bei kathodischer Wasserstoffentwicklung, Zeitschrift Für Physikalische Chemie 50 (1905) 641–712.

[32] H. Strathmann, H.J. Rapp, B. Bauer, C.M. Bell, Theoretical and practical aspects of preparing bipolar membranes, Desalination 90 (1993) 303–323, https://doi.org/10.1016/0011-9164(93)80183-N.

[33] P. Fievet, Donnan Effect, in: Encyclopedia of Membranes, Springer Berlin Heidelberg, 2014: pp. 1–3. https://doi.org/10.1007/978-3-642-40872-4_1714-1.

[34] L. Chen, Q. Xu, S.W. Boettcher, Kinetics and mechanism of heterogeneous voltage-driven water-dissociation catalysis, Joule 7 (2023) 1867–1886, https://doi.org/10.1016/J.JOULE.2023.06.011.

[35] A. Einstein, Über die von der molekularkinetischen Theorie der Wärme geforderte Bewegung von in ruhenden Flüssigkeiten suspendierten Teilchen, Ann Phys 322 (1905) 549–560.

[36] S. Honarparvar, D. Reible, Modeling multicomponent ion transport to investigate selective ion removal in electrodialysis, Environmental Science and Ecotechnology 1 (2020) 100007, https://doi.org/10.1016/J.ESE.2019.100007.

[37] F.G. Donnan, The theory of membrane equilibria, Chem Rev 1 (1924) 73–90, https://doi.org/10.1021/CR60001A003.

[38] H. Fan, Y. Huang, I.H. Billinge, S.M. Bannon, G.M. Geise, N.Y. Yip, Counterion Mobility in Ion-Exchange Membranes: Spatial Effect and Valency-Dependent Electrostatic Interaction, ACS ES and T Engineering 2 (2022) 1274–1286.

[39] A.R. Khare, N.A. Peppas, Swelling/deswelling of anionic copolymer gels, Biomaterials 16 (1995) 559–567, https://doi.org/10.1016/0142-9612(95)91130-Q.

[40] A.E. Kozmai, V.V. Nikonenko, S. Zyryanova, N.D. Pismenskaya, L. Dammak, A simple model for the response of an anion-exchange membrane to variation in concentration and pH of bathing solution, J Memb Sci 567 (2018) 127–138, https://doi.org/10.1016/J.MEMSCI.2018.07.007.

[41] M. von Smoluchowski, Zur kinetischen Theorie der Brownschen Molekularbewegung und der Suspensionen, Ann Phys 326 (1906) 756–780.

[42] H. Roux-de Balmann, M. Bailly, F. Lutin, P. Aimar, Modelling of the conversion of weak organic acids by bipolar membrane electrodialysis, Desalination 149 (2002) 399–404, https://doi.org/10.1016/S0011-9164(02)00863-9.